First 3D test particle model of Ganymede's ionosphere

Gianluca Carnielli, Marina Galand, François Leblanc, Ludivine Leclercq, Ronan Modolo, Arnaud Beth, Hans L. F. Huybrighs, Xianzhe Jia

First 3D test particle model of Ganymede's ionosphere

G. Carnielli[a,*], M. Galand[a], F. Leblanc[b], L. Leclercq[c], R. Modolo[d], A. Beth[a], H. L. F. Huybrighs[e], X. Jia[f]

[a]*Department of Physics, Imperial College London, SW7 2AZ, London, United Kingdom*
[b]*LATMOS/IPSL, CNRS, Sorbonne Université, UVSQ, Paris, France*
[c]*University of Virginia, Charlottesville, Virginia, USA*
[d]*LATMOS/IPSL, UVSQ Université Paris-Saclay, UPMC Univ. Paris 06, Guyancourt, France*
[e]*ESA/ESTEC, Noordvijk, The Netherlands*
[f]*Department of Climate and Space Sciences and Engineering, University of Michigan, Ann Arbor, MI 48109-2143, USA*

Abstract

We present the first three-dimensional multi-species ionospheric model for Ganymede, based on a test particle Monte Carlo approach. Inputs include the electromagnetic field configuration around the moon from the magnetospheric models developed by Leclercq et al. (2016) and by Jia et al. (2009), and the number density, bulk velocity and temperature distributions of the neutral exosphere simulated by Leblanc et al. (2017). According to our simulations, O_2^+ is the most abundant ion species, followed by O^+, H_2^+ and H_2O^+. For O^+ and O_2^+, the majority of ions produced impact the moon's surface, while for the other species the majority escapes Ganymede's magnetosphere. For all ion species, the escape occurs either in the direction of corotation of the Jovian plasma or through the Alfvén wings.

To validate our model, the output of our simulations, performed under the Galileo G2 flyby conditions, are compared to the observations. These include the electron density derived by the plasma wave instrument (PWS), the ion

*Principal corresponding author:
Email address: gianluca.carnielli10@imperial.ac.uk (G. Carnielli)

energy spectrogram measured by the plasma analyzer (PLS) and the associated plasma moments (Frank et al. (1997a)). On the one hand, the electron density found by our model is consistently underestimated throughout the flyby, being at least one order of magnitude lower compared to observations. We argue that the prime reason for this discrepancy comes from the exospheric density, which may be underestimated. On the other hand, we find a remarkably good agreement between the modeled ion energy spectrogram and that recorded by PLS, providing a validation of the test particle model. Finally, we compare the modeled plasma moments along the G2 flyby with those analyzed by Frank et al. (1997a). The data seems to be more consistent with an ionosphere dominated by O_2^+ instead of H^+ or O^+, as suggested previously in the literature. This supports our finding that O_2^+ is the dominant ion species close to the surface.

Keywords: Ganymede, Ionospheres, Jupiter, satellites, Satellite, atmospheres

1. Introduction

Ganymede is the largest amongst the Galilean satellites and the prime target of the JUpiter ICy moons Explorer (JUICE) mission (Grasset et al. (2013)). Besides being the largest moon in the Solar System, it is also the only one known to generate a magnetic field which is strong enough to overcome the background Jovian field (Kivelson et al. (1996, 1997)); thus, the moon carves out its own magnetosphere inside that of Jupiter.

The moon's magnetosphere is shaped by the dynamic interaction between its internal dipole field and the Jovian plasma which overtakes the moon from

the orbitally trailing hemisphere at a speed of around 140 km/s in the moon's frame (Kivelson et al. (2004)). At Ganymede's orbital radius (∼15 Jupiter radii) the plasma sheet corotates with Jupiter with a synodic period of 10.5 hours. Due to the relative inclination between Ganymede's orbital plane and the magnetic equatorial plane of Jupiter, the moon orbits periodically above and below the plasma sheet. This causes a periodic change of the background magnetic field and upstream plasma conditions. Several MHD and hybrid models have been developed to study the interaction between Ganymede's internal field and the Jovian plasma sheet (Jia et al. (2008, 2009); Ip and Kopp (2002); Paty and Winglee (2006); Leclercq et al. (2016); Wang et al. (2018)). The models show that the interaction between the sub-sonic and sub-Alfvénic flow and the moon's magnetic field leads to the formation of Alfvén wings at the poles and a region of closed magnetic field lines at lower latitudes.

Past remote and in-situ observations of the moon provided evidence of the existence of a thin atmosphere. Barth et al. (1997) reported on the detection of hydrogen from the ultraviolet spectrometer (UVS) onboard the Galileo spacecraft, while Hall et al. (1998) and Feldman et al. (2000) inferred the presence of O and O_2 from observations of Ganymede's aurora with the Hubble Space Telescope (HST). The exosphere is primarily formed from surface sputtering and radiolysis by energetic Jovian ions in the polar regions and by sublimation of the icy surface in the subsolar region. Several exospheric models have been developed to describe the neutral environment around the moon. Marconi (2007), Turc et al. (2014), Plainaki et al. (2015) and Shematovich (2016) predicted an exosphere dominated by O_2 in the po-

lar region and by H_2O in the subsolar region, while the most recent model of Leblanc et al. (2017) considered a low sublimation rate in the subsolar region, making, O_2 the dominant species everywhere at low altitudes.

The ionosphere is formed by ionization of the neutral exosphere. This occurs primarily by absorption of solar EUV radiation and electron impact from the Jovian magnetosphere population. Kliore (1998) provided an upper limit of 4000 cm^{-3} for the ionospheric density from a Galileo radio occultation, while Eviatar et al. (2001) presented electron density profiles from the Plasma Wave Science (PWS) instrument along the G1 and G2 flyby trajectories, consistent with the upper limit of Kliore (1998). Frank et al. (1997b) presented measurements of an ion outflow recorded by the Plasma Science instrument (PLS) onboard Galileo. They interpreted it as H^+ leaving Ganymede's magnetosphere, in agreement with the finding of the multi-fluid MHD simulation of Paty et al. (2008), who found O^+ to have an energy below the instrument threshold, leaving it undetected. Vasyliūnas and Eviatar (2000) reinterpreted this population as being O^+ with four times the number density and one quarter of the speed.

Previous ionospheric models include those from Eviatar et al. (2001) and Cessateur et al. (2012). Both used a simplified chemical model and zero-dimensional local rate equations to retrieve the ionospheric density profile. These models rely on a number of too restrictive assumptions, such as the lack of transport for Cessateur et al. (2012) and ion composition reduced to O^+ and O_2^+ for Eviatar et al. (2001).

We have developed the first 3D model of Ganymede's ionosphere, which generates 3D high resolution maps of the number density, bulk velocity and

temperature for different species in Ganymede's ionosphere. The results from our model can be used not only to make more realistic interpretations of Galileo ionospheric data during Ganymede's flybys, but also to support the JUICE mission. In addition to providing support for the interpretation of data that will come from the spacecraft, the results of our model can be used for optimising the operation mode of some instruments such as the Radio Plasma Wave Instrument (RPWI). Furthermore, our model provides a set of results, such as the plasma distribution around the moon, which can be used in magnetospheric models to improve on the short comings of assumptions adopted, such as the spherically symmetric configuration of the ionospheric plasma.

In Section 2, we describe the ionospheric model, including the algorithm and the major drivers. In Section 3, we present the conditions assumed for the simulation and the assumptions made. In Section 4, we present the results of our simulations over selected regions. In Section 5.1, our results are compared with Galileo observations during G2 and in Section 5.2 reasons for differences are discussed. Section 6 highlights the main results and their implications.

2. The model

The ionospheric model is based on a Monte Carlo approach, where test particles, i.e., macro particles representing a certain physical number of ions, are created and followed in the presence of electric and magnetic fields. The simulation is undertaken on a spherical grid centered on Ganymede containing $100 \times 90 \times 180$ cells in the radial (r), polar (θ) and azimuthal (ϕ) directions,

respectively. The radial cells extend from the surface up to 6.7 R_g ($R_g \equiv$ Ganymede's radius $\equiv$ 2634.1 km) with spacing between cells increasing with altitude, while the cells in the polar and azimuthal directions are equally spaced with a separation of 2°. A total of 7.1×10^7 test particles launched was found to suffice in order to obtain statistically robust results.

The model has two main inputs which are read at the start of the simulation:

- the electric and magnetic fields around Ganymede, defined on a square grid with a resolution of 125 km between |X|, |Y| and |Z| $\leq$ 4 R_G and of 250 km between 4 R_G < |X|, |Y|, |Z| < 8 R_G. These are outputs of the hybrid model developed by Leclercq et al. (2016) and applied to the Ganymede environment;

- the neutral number density, bulk velocity and temperature of different species from the exospheric model of Leblanc et al. (2017), defined on a spherical grid centered on Ganymede with the same radial range but with different θ and ϕ distributions compared to the ionospheric grid. The neutral species n considered are O_2, H_2O, H_2, H, O, OH.

The ionosphere is created from ionization of the neutral exosphere. During a given simulation, one ion species i (O_2^+, OH^+, H^+, H_2^+, H_2O^+ and O^+) is produced. The test particles representing ion i are created at random positions in every cell of the exospheric grid where they get assigned a weight and an initial velocity. The weight, W_j, equals the number of physical particles represented by the test particle, and is assigned according to the following formula:

$$W_j = dt \times V_{cell,exo} \times \sum_n n_n \times \nu_{i,n} \tag{1}$$

where dt is the timestep, $V_{cell,exo}$ is the volume of the cell of the exospheric grid, n_n is the number density of the neutral species n in the cell where the macro-particle is produced and $\nu_{i,n}$ is the ionization frequency of the ion species i generated from the ionization of the neutral n (see Section 3.1).

The initial velocity of the test particle, $\vec{v}_j(t=0)$, is assigned in relation to the average velocity $\vec{v}_n$ of the neutral species in the cell where the particle is produced, according to the following equation:

$$\vec{v}_j(t=0) = \frac{\sum_n n_n \times \nu_{j,n} \times \left(\vec{v}_n \pm R\sqrt{2k_B T_n/m_j}\right)}{\sum_n n_n \times \nu_{j,n}} \tag{2}$$

where the sum is over all neutral species n whose ionization can lead to the ion species i, T_n is the temperature of the neutral species n and R is a uniformly distributed random number between 0 and 1 that generates the velocity dispersion for the ionospheric species. Although this is an average of the range of possible ion velocities, it turns out that the exact value of this parameter is irrelevant since the ions are quickly accelerated by the ambient electric and magnetic fields to speeds which are significantly higher compared to the speeds of the neutral species. A test simulation was performed, where a null velocity was assigned to the test particles, and the effect on the results was negligible.

The newborn test particle j is thus subject to the Lorentz force (gravity was verified to have a negligible effect on the motion), yielding:

$$m_j \frac{\mathrm{d}\vec{v_j}}{\mathrm{d}t} = q_j(\vec{E} + \vec{v}_j \times \vec{B}) \tag{3}$$

where $\vec{E}$ and $\vec{B}$ are the electric and magnetic fields, respectively, m_j is the ion's mass and q_j the electric charge of the test particle. We tested different algorithms with an adaptive timestep to integrate Equation 3, including Euler, RK4 and Boris (Boris (1970)). The results did not change significantly between different algorithms, so we opted for the Boris scheme owing to its lower computational cost. We are aware that Skeel and Gear (1992) warned that Verlet-like algorithms - which Boris belongs to - can be unstable if used with an adaptive timestep. However, we applied this scheme to the field environment around Ganymede and found no noticeable difference in the results compared with a simulation that used the same algorithm but with a fixed timestep. Due to the significantly reduced computation time involved in a simulation with adaptive timestep, we chose to stick with this method. At each iteration the timestep is calculated to meet the following criteria:

- The distance travelled by the test particle must not exceed the size of the surrounding ionospheric grid cells, such that cells are not skipped from one timestep to the next (also known as 'CFL condition');
- The distance travelled by the test particle must not exceed the resolution of the hybrid grid, such that particles feel the correct Lorentz force down to the resolution of the hybrid grid;
- The test particle must not travel more than $1/20^{\mathrm{th}}$ of the instant gyroradius in order to simulate a sufficiently realistic path.

The test particles are followed until either they impact the moon's surface or they cross the outer boundaries of the simulation grid. Throughout the trajectory, the weight and the velocity of the test particle are saved in each cell that the particle traversed. At the end of the simulation, when all test particle trajectories have been simulated, the number density $n_{i,cell}$, bulk velocity $\vec{u}_{i,cell}$, and temperature $T_{i,cell}$ of the ion species simulated are calculated for each cell according to the following equations:

$$n_{i,cell} = \frac{\sum_j W_j}{V_{cell,iono} \times N_{stat}}, \tag{4}$$

$$\vec{u}_{i,cell} = \frac{\sum_j \vec{v_j} \times W_j}{\sum_j W_j}, \tag{5}$$

$$T_{i,cell} = \frac{m_i}{3k_B} \left(\frac{\sum_j |\vec{v_j}|^2 \times W_j}{\sum_j W_j} - |\vec{u}_{i,cell}|^2 \right) \tag{6}$$

where $V_{cell,iono}$ is the volume of the ionospheric grid cell, N_{stat} is a statistical parameter representing the number of test particles injected initially per exospheric grid cell, k_B is the Boltzmann's constant, and W_j and $\vec{v_j}$ are the weight and velocity, respectively, of the test particles deposited at each iteration in the cell. The sums run over all iterations and test particles. 3D maps of these quantities are generated separately for each ion species.

The simulation records also the individual test particle trajectories, allowing an easier physical interpretation of the 3D maps.

3. Simulation inputs and model assumptions

We present here the inputs for the simulations. These include: the sources for the ionization processes (Section 3.1) the configuration of the exosphere

Jupiter's local time	10 AM
Solar flux activity	minimum
Jupiter heliocentric distance	5.46 AU
Location of Ganymede with respect to the plasma sheet	Above
Background magnetic field (nT)	(0,-79,-79)

Table 1: Simulation conditions assumed in our model which are based on the Galileo G2 flyby.

from the model of Leblanc et al. (2017) (Section 3.2) and the configuration of the magnetosphere (Section 3.3). The model assumptions are described in Section 3.4. For the maps in Sections 3 and 4 we use the GPhiO coordinate system, centered on Ganymede, in which the X-axis points to the direction of corotation of the Jovian plasma (which is also the direction of Ganymede's orbital motion), the Y-axis points towards Jupiter and the Z-axis completes the right-handed coordinate system. For the simulations we chose, to reproduce Ganymede's environment during the G2 flyby to compare our results with observations (see Section 5). Table 1 provides a list of the conditions that were assumed.

3.1. Ionization sources

3.1.1. Photo-ionization

Ganymede's sunlit exosphere is constantly photo-ionized by solar EUV radiation. The photo-ionization frequency of the ion species i, ν_i^{γ}, is calculated as follows:

$$\nu_i^{\gamma} = \sum_n \int_0^{\lambda_{th}} \mathrm{d}\lambda \; I^{\infty}(\lambda) \times \sigma_{i,n}^{ion}(\lambda) \tag{7}$$

where λ is the radiation wavelength, λ_{th} is the threshold wavelength for ionization, $\sigma_{i,n}^{ion}(\lambda)$ is the ionization cross-section of the neutral n, producing the ion species i, $I^{\infty}(\lambda)$ is the unattenuated solar radiation spectral flux at Ganymede's orbit and the sum runs over all neutral species which produce i.

The solar activity was close to its minimum at the time of the G2 flyby (see Table 1), hence we used a corresponding solar flux. The data for the solar radiation flux was obtained from the TIMED/SEE database (http://lasp.colorado.edu/see/, Woods et al. (2005)) at 1 AU and extrapolated to Jupiter's orbital distance at 5.46 AU.

Table 2 provides the list of ionization processes considered in our model, along with the reference for ionization cross-sections and associated ionization frequencies. The photo-ionization frequencies were compared to those reported by Huebner and Mukherjee (2015) at low solar activity, and were found to be in good agreement (within 10%).

3.1.2. Electron impact

The Jovian plasma is able to partially penetrate inside Ganymede's magnetosphere, and the energetic electrons ($>$ tens of eV) are able to ionize the neutral exosphere. Unfortunately, no data is available for the combined spatial and energetic distribution of electrons inside the magnetosphere. We would expect an asymmetry in the energy distribution between the open and closed magnetic field line regions. In particular, in the region of closed magnetic field lines we would expect mainly low energy electrons to be present

Table 2: List of ionization reactions, the respective ionization frequencies, considered in the ionospheric model and calculated with the cross-sections referenced in the 3rd column. Electron-impact processes, frequency values and references are given in parenthesis. The photo-ionization frequencies were calculated at solar minimum conditions and given at the location of Jupiter (see Section 3.1).

Ionization by solar photons (electrons)	$\nu^{h\nu}$ (ν^{e}) $[10^{-8}$ s$^{-1}]$	Ref.
$H + h\nu\ (e^-) \rightarrow H^+ + e^-\ (+\ e^-)$	0.24 (2.41)	1
$H_2 + h\nu\ (e^-) \rightarrow H_2^+ + e^-\ (+\ e^-)$	0.23 (3.02)	2
$H_2 + h\nu\ (e^-) \rightarrow H + H^+ + e^-\ (+\ e^-)$	0.01 (0.24)	2
$H_2O + h\nu\ (e^-) \rightarrow H_2O^+ + e^-\ (+\ e^-)$	1.13 (4.25)	3
$H_2O + h\nu\ (e^-) \rightarrow H + OH^+ + e^-\ (+\ e^-)$	0.23 (1.29)	3
$H_2O + h\nu\ (e^-) \rightarrow O^+ + H_2 + e^-\ (+\ e^-)$	0.02 (0.19)	3
$H_2O + h\nu\ (e^-) \rightarrow H^+ + OH + e^-\ (+\ e^-)$	0.11 (1.03)	3
$O + h\nu\ (e^-) \rightarrow O^+ + e^-\ (+\ e^-)$	0.87 (4.90)	4
$O_2 + h\nu\ (e^-) \rightarrow O_2^+ + e^-\ (+\ e^-)$	1.75 (9.05)	5
$O_2 + h\nu\ (e^-) \rightarrow O + O^+ + e^-\ (+\ e^-)$	0.44 (0.90)	5
$OH + h\nu\ (e^-) \rightarrow OH^+ + e^-\ (+\ e^-)$	1.75 (5.76)	6

[1] Verner et al. (1996) (Galand et al. (2009))

[2] Galand et al. (2009) (Galand et al. (2009))

[3] Vigren and Galand (2013) (Itikawa and Mason (2005))

[4] Cui et al. (2011) (Laher and Gilmore (1990))

[5] 0-1.5 nm: Branching ratio of Stolte et al. (1998) applied to the photo-absorption cross-section from Avakyan (1998); 1.5-12 nm: Stolte et al. (1998); 12-50 nm: Brion et al. (1979); above 50 nm: Schunk and Nagy (2004). (Straub et al. (1996))

[6] Photo-ionization rate of OH was set equal to that of H_2O, after Schreier et al. (1993) (Joshipura et al. (2001))

from photo-ionization of the neutral atmosphere, and not energetic electrons from the Jovian plasma sheet which are not able to penetrate (Williams et al. (1998)). Due to our limited knowledge of the electron population inside Ganymede's magnetosphere, ionization from Jovian electrons is assumed to take place only within the region of open magnetic field lines. The energy distribution of the Jovian electrons is set to be spatially constant within this simulation volume. The ionization frequency, ν_i^e, is calculated as follows:

$$\nu_i^e = \sum_n \int_{E_{th}}^{E_{max}} \mathrm{d}E \; I(E)\sigma_{e,n}^{ion}(E) \tag{8}$$

where E is the electron energy, E_{th} is the energy threshold for electron-impact ionization, E_{max} is the highest electron energy available from data, $I(E)$ is the electron differential flux and $\sigma_{e,n}^{ion}(E)$ is the energy-dependent ionization cross-section for the electron impact on the neutral species n producing the ion i. The sum runs over all neutral species n whose electron-impact ionization can lead to i.

Our approach differs from that of Marconi (2007) and Turc et al. (2014), who assumed a constant electron number density of 70 cm^{-3} (only in the polar region in the model of Turc et al. (2014)) and temperature of 20 eV in relation to exospheric loss processes. The value for the number density corresponds to the average between measurements taken during the G1 and G2 flybys and extrapolated to 0.2 R_G, while the electron temperature corresponds to that measured at Europa. By taking the moments of the black, dashed distribution in Figure 1 (integrating from 14 eV to 5.16 keV), one obtains a density of 0.76 cm^{-3} and a temperature of around 140 eV. The density is significantly lower compared to that used in the exospheric models, which

instead relied on measurements that captured the full electron population, i.e., including electrons with energies below 14 eV. As a result, the electron-impact ionisation frequencies obtained with our approach are lower by more than one order of magnitude.

Furthermore, based on the differential cross-section relation from Opal et al. (1971) for electron-impact ionization, most of the secondary electrons produced were found to have energies which are either lower than the ionization threshold of the neutral species or low enough to be in the part of the energy spectrum where the ionization cross-section is low. As a result, most of the secondary electrons would not be able to efficiently ionize: we have neglected their contribution in the model.

To simulate the ionization from electron impact we combined the electron energy distributions outside Ganymede's magnetosphere and away from the plasma sheet from Scudder et al. (1981) and Paranicas et al. (1999), as shown in Figure 1. We also verified that the electron flux presented by Cooper et al. (2001) (who used data from the Galileo EPD instrument) and Paranicas et al. (1999) (who used data from both the Galileo PLS and EPD instruments) are consistent between each other, as both presented data for the G2 flyby.

The ionization frequencies calculated for electron-impact are given in Table 2. We found for all neutral-ion pair considered that electron-impact ionization dominates over photo-ionization in the region of open magnetic field lines, where both ionizing sources are active (electron impact is not included in the region of closed magnetic field lines).

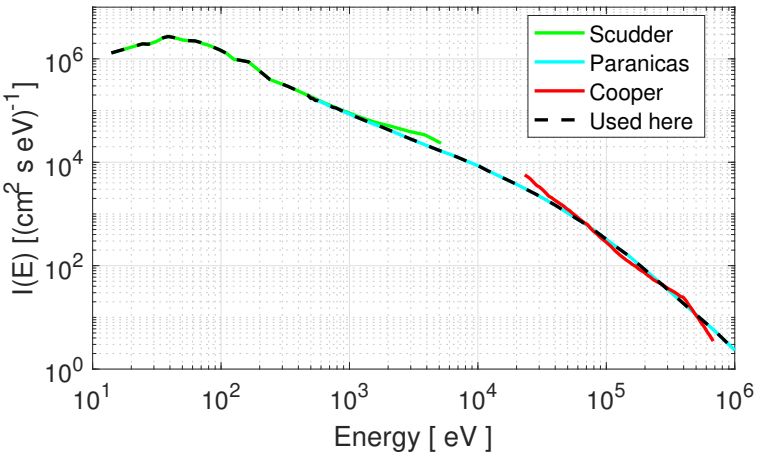

Figure 1: Electron differential flux as a function of energy, outside the Jovian plasma sheet near Ganymede. Isotropy was assumed. The green curve shows the flux computed from the distribution function in Scudder et al. (1981) adapted to Ganymede's orbital distance, the cyan curve shows the flux presented in Paranicas et al. (1999), the red curve shows the flux presented in Cooper et al. (2001) and the dashed black curve shows the combined flux adopted in our simulation.

3.2. Exosphere

The exospheric model of Leblanc et al. (2017) simulates the dynamical variation of the exosphere as Ganymede revolves around Jupiter. This affects the ionosphere because the spatial distribution of the neutral species changes in Ganymede's reference frame along with the location of the illuminated region.

Figure 2 shows in the XZ plane the number density maps of the three major neutral species, O_2, H_2 and H_2O, from the exospheric model of Leblanc et al. (2017). O_2 is dominant close to the surface, followed by H_2, since these are the only species that do not stick to the surface. At higher altitudes, the

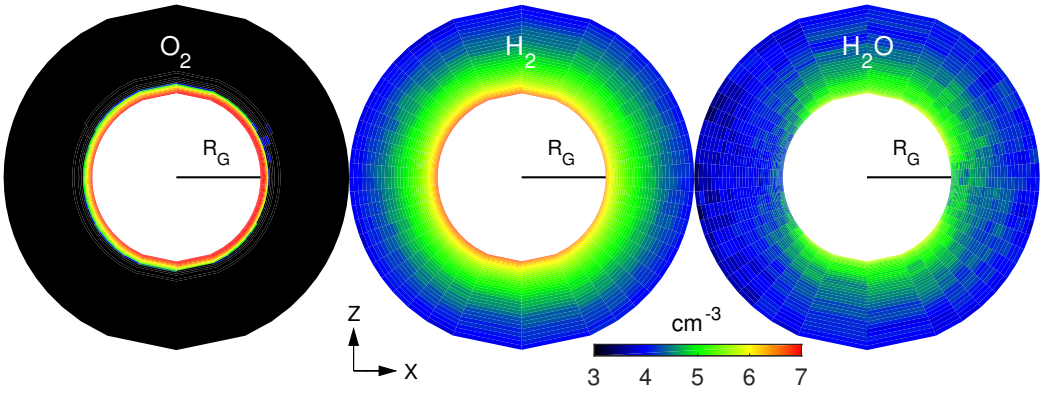

Figure 2: Number density profile of the major neutral species in the XZ plane, from the exospheric model of Leblanc et al. (2017) when Ganymede is at 10 AM in Jupiter's local time.

exosphere is dominated by H_2 and H_2O. There is an asymmetry between the dawn and dusk sectors, with the dusk sector achieving the highest densities (not shown). O_2 and H_2, by not sticking to the surface, can accumulate near the surface. They are primarily produced on the day side (sputtering being surface-temperature dependent), where they bounce on the surface, and destroyed in the night side where their residency time is larger due to a lower surface temperature. Destruction on the night side occurs in the region of open magnetic field lines where electron-impact ionisation and dissociation are turned on. Leblanc et al. (2017) also showed that O_2 molecules move very slowly in Ganymede's frame (with respect to ionization lifetime) so that they accumulate on the day side, leading to a peak of density at dusk. It is less true for H_2 because its motion in Ganymede's frame is much faster.

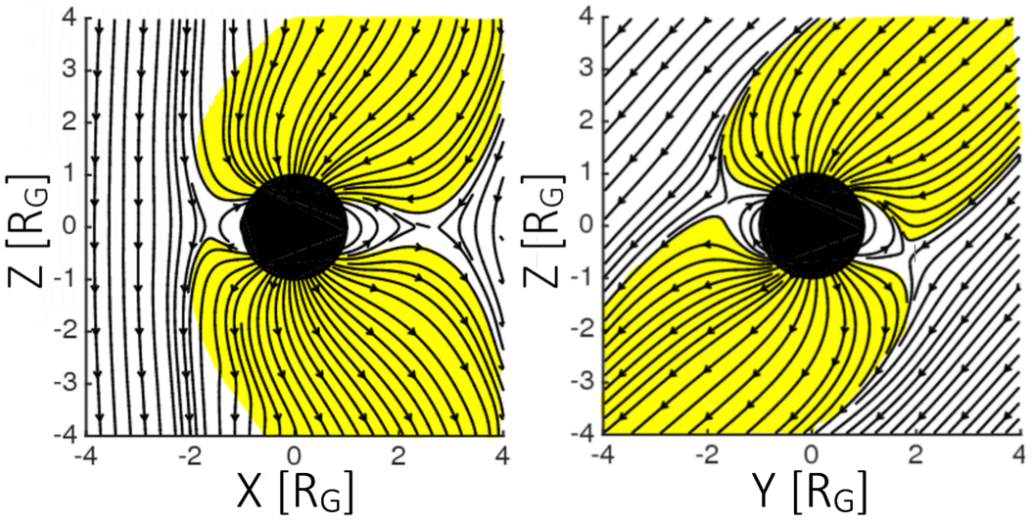

Figure 3: Magnetic field configuration around Ganymede above the plasma sheet from the hybrid model of Leclercq et al. (2016). 1 RG ≡ 1 Ganymede's radius ≡ 2634 km. The yellow region represents the cut of the Alfvén wings in each plane.

3.3. Magnetosphere configuration

To simulate Ganymede's magnetosphere we used the hybrid model of Leclercq et al. (2016) applied to Ganymede under G2 conditions, which are listed in Table 1. We checked that the lifetime of ionospheric species in the simulation is typically a few minutes. In this time frame the magnetosphere does not change significantly, so it is safe to assume a constant configuration of the electric and magnetic fields throughout the simulation.

Figure 3 shows a portion of the magnetic field topology used as input to the ionospheric model. The yellow regions correspond to the section of the Alfvén wings that intersect each plane. The magnetic field lines are bent by 45° with respect to the Z-axis and point away from Jupiter as Ganymede is above the plasma sheet.

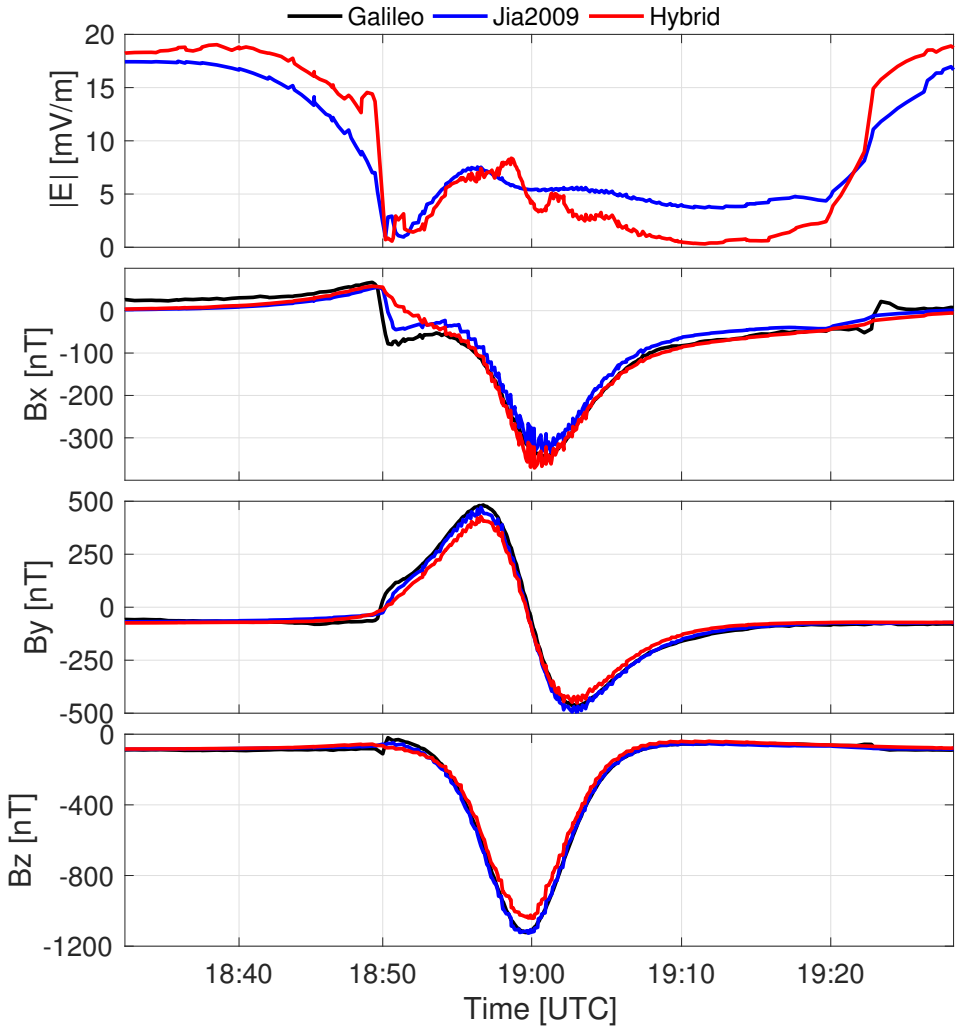

Figure 4: Comparison of the simulated electric field magnitude (top panel) and magnetic field components (bottom panels) along the G2 trajectory between the hybrid simulation of Leclercq et al. (2016) (red curve) and the MHD simulation of Jia et al. (2009)(blue curve). For the magnetic field components, the observed values are shown by the black curve.

To study how the results from the test particle model are influenced by the input fields, we have also run simulations using the fields from the MHD model of Ganymede's magnetosphere developed by Jia et al. (2009). This model makes some different assumptions compared to the hybrid model, including the plasma composition and the boundary conditions at the ionospheric layer and upstream injection plane. The hybrid model of Leclercq et al. (2016) simulated two Jovian plasma species with different fractional compositions: O^+ (87%) and H^+ (13%). The plasma density at the upstream injection plane was set to 4 cm^{-3} to match the Jovian plasma sheet electron density reported by Gurnett et al. (1996), and the ionosphere was prescribed a number density at the surface of 500 cm^{-3} with an exponential decay governed by a scale height of 125 km. The ionosphere was assumed to be composed of O^+ only, with a spherically symmetric configuration. In the MHD model of Jia et al. (2009) the Jovian plasma was simulated as a single fluid with density of 28 AMU/cm^3, which corresponds to less than 2 cm^{-3} if O^+ is assumed. For the ionospheric boundary layer, their model assumed a density of 550 AMU/cm^3, which corresponds to a number density of around 34 cm^{-3} if O^+ is assumed. The different choices for the input conditions lead to some differences in the field configurations, in particular close to the surface (later discussed in Section 5).

The top panel of Figure 4 shows the magnitude of the electric field along the G2 trajectory as found by the hybrid and MHD models. The other three panels of Figure 4 show the comparison of the Cartesian components of the magnetic field with Galileo measurements. Overall, the magnetic field simulated by both models features a close correspondence with the observed

values for all three **B** field components. Between the two models, the MHD simulation finds a better agreement with observations. For the hybrid model, departures from observations occur near the magnetopause boundary crossings at 18:50 UTC and 19:22 UTC for the x-component, and a slight shift between data and simulated values is seen near closest approach at 19:00 UTC for the y- and z- components. Further comparison between the two models are highlighted in Section 5.

3.4. Model assumptions

3.4.1. Optically thin approximation

In dense atmospheres the solar radiation gets absorbed by the neutral gas. The initially unattenuated spectral flux decreases as the radiation penetrates deeper in the atmosphere, according to the Beer-Lambert law:

$$I(\vec{r},\lambda) = I^{\infty}(\lambda) \times e^{-\tau(\vec{r},\lambda)} \tag{9}$$

where $I^{\infty}(\lambda)$ is the unattenuated solar spectral flux, λ, the radiation wavelength, $\vec{r}$, the position vector and τ is the optical depth which parametrizes the absorption factor. It is defined as:

$$\tau(\vec{r},\lambda) = \sum_{n} \sigma_n^{abs}(\lambda) \int_{s(\vec{r})}^{\infty} \mathrm{d}s' \; n_n(s') \tag{10}$$

where σ_n^{abs} is the photo-absorption cross-section for the neutral species n and $n_n(\vec{r})$ its number density. The integral is over the line of sight - associated with abscissa s' - from s at position $\vec{r}$ to the solar direction and the sum includes all neutral species present along the line of sight. If τ is close to 0 at a given position and wavelength then the solar radiation is

unattenuated: the atmosphere is optically thin for that wavelength at that position.

From the number density maps obtained from the exospheric model of Leblanc et al. (2017) we calculated τ for Ganymede's exosphere. Figure 5c shows the absorption cross-sections that were used to calculate the optical depth for O_2, H_2 and H_2O, the major species present in Ganymede's neutral atmosphere. In terms of number density, O_2 dominates below 160 km, while H_2 and H_2O dominate above that. For O_2, the absorption cross-section peaks at 63 nm, while for H_2 the peak is at 98 nm, as seen in Figure 5c. The relative abundance of these two species leads to a peak of approximately 0.03 in the optical depth at 63 nm (see Figure 5a) in the polar region (see Figure 5b). A maximum optical depth of 0.03 implies that even at the surface the solar intensity is not significantly attenuated. This result applies over the full longitude range. Therefore, it is justified to assume the exosphere to be optically thin: the solar radiation intensity is the same everywhere in the simulation volume, except in the night side where it is absent. This translates into a spatially constant photo-ionization frequency over the sunlit region of the simulation domain, which we have assumed in our model.

3.4.2. Collisional and chemical properties of the ionosphere

The ionospheric species can undergo chemical reactions and collisions with the atmospheric neutral species. To assess how important these processes are for each ion species in each cell of the simulation grid, the ion's chemical lifetime was compared with its transport timescale. The chemical lifetime of an ion species i is given by:

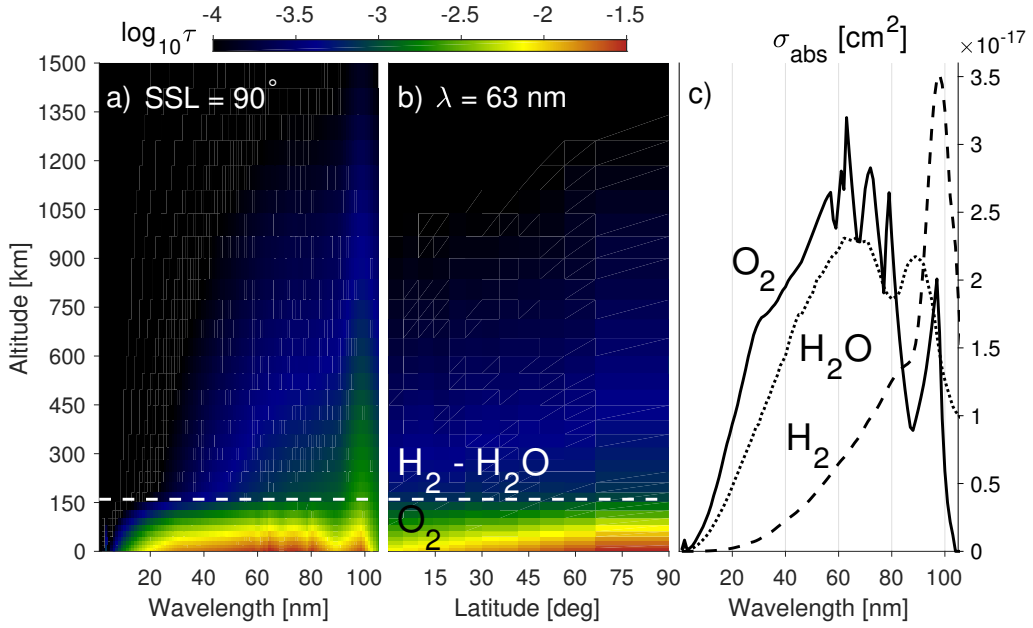

Figure 5: a) Optical depth at the North pole as a function of altitude (y-axis) and wavelength (x-axis). b) Optical depth at the subsolar longitude as a function of altitude (y-axis) and latitude (x-axis) for $\lambda = 63$ nm. 0° corresponds to the equator and 90° to the North pole. c) Absorption cross-section as a function of wavelength for O_2,H_2 and H_2O. References for O_2 cross-section values: 0-1.5 nm: Branching ratio of Stolte et al. (1998) applied to the photo-absorption cross-section from Avakyan (1998); 1.5-12 nm: Stolte et al. (1998); 12-50 nm: Brion et al. (1979); above 50 nm: Schunk and Nagy (2004). Reference for H_2 cross-section values: Backx et al. (1976). Reference for H_2O cross-section values: Vigren and Galand (2013).

$$\tau_{i,k}^{chem} = \frac{1}{\alpha_{i,k} n_k} \tag{11}$$

where $\alpha_{i,k}$ is the coefficient rate of the chemical reaction considered between the ion species i and atmospheric species k, in cm^3 s^{-1}, and n_k is the number density of k, in cm^{-3}. The species k can be exospheric (ion-neutral

reaction) or an electron (ion-electron dissociative recombination). This calculation was done for all major chemical reactions between the ionospheric ions and the exospheric species or electrons. Reactions involving charge-exchange were also considered, as simple momentum transfer collisions are inefficient for typical energies of Ganymede's ionospheric ions, above 0.1eV (Banks (1966)). To calculate the transport timescale in each cell we computed the time taken by the ion to travel a distance equal to the local ion scale height H_i, i.e.:

$$\tau_i^{tran} = \frac{H_i}{u_{i,cell}} \tag{12}$$

where $u_{i,cell}$ is the ion bulk velocity derived from a simulation assuming a collisionless ionosphere and $H_i = n_i/|(\mathrm{d}n_i/\mathrm{d}r)|$ where n_i is the ion number density.

Figure 6 shows a comparison between the timescales for transport and reactions with the neutral species for the case of O^+ and O_2^+, the major constituents of the ionosphere (see Section 4). The calculation was carried out in three distinct regions: the northern polar region, the equatorial region and the southern polar region. These are separated by the open-close field line boundaries (OCFLB) at mid-latitudes, shown as solid, black lines in the top panels of Figure 6. The ion scale height and velocity were taken from a run of our model which assumed no interaction with the neutral exosphere, and the exospheric densities were taken from the model of Leblanc et al. (2017) (the modeled exosphere used was the "low sublimation" case, in which no semi-dense H_2O atmosphere forms in the subsolar region, see Section 2.3 in Leblanc et al. (2017)). For each region and each altitude, the plotted

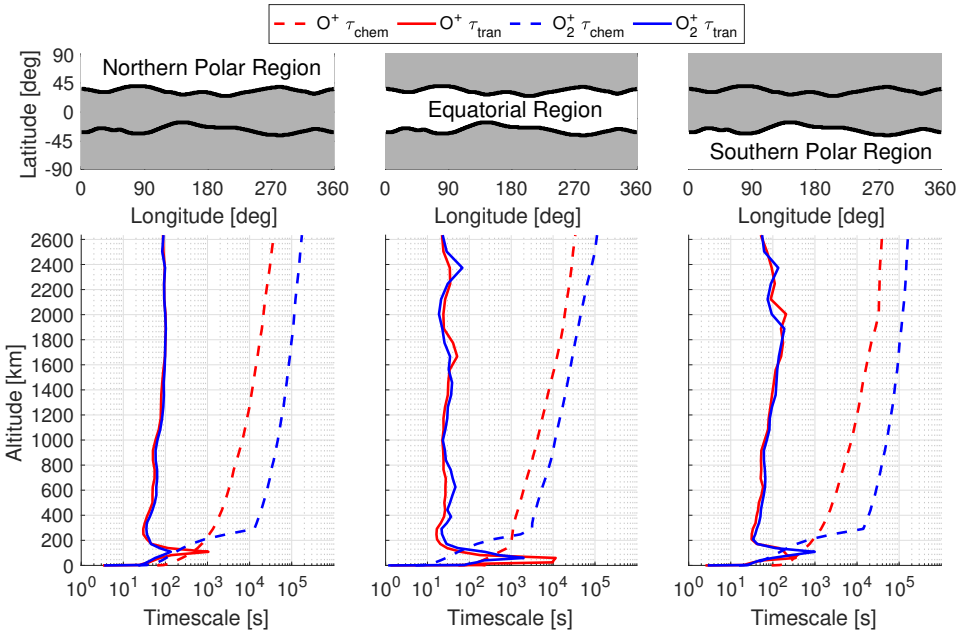

Figure 6: Top: Maps indicating the latitude-longitude domain of calculation considered for the plots in each respective bottom panel. The regions are separated by the open-close magnetic field line boundaries, plotted as solid, black lines. The white area corresponds to the domain of calculation, while the grey area shows the excluded regions. Bottom: Plots of the chemical (τ_{chem}) and transport (τ_{tran}) timescales of O^+ (red) and O_2^+ (blue) as functions of altitude. For each region and each altitude, the plotted value corresponds to the average over all longitudes and latitudes within the calculation domain, shown by the white area on the top panel. Solid lines correspond to transport timescales, and dashed lines correspond to chemical timescales, corresponding to charge exchange (as timescales associated with ion-neutral collisions are larger).

value is the average over all longitudes and latitudes within that region (the white area in the top panels of Figure 6). This is justified as the ionospheric parameters, such as density and velocity, in that altitude range (0 to 2600 km) differ primarily between regions and not longitude (see Section 4.2.1) due to the configuration of the electromagnetic field (see Section 3.3).

The profiles for the chemical timescale are found to increase for both ions as a function of altitude in all regions, in concomitance with the decreasing density of exospheric species. Below 200 km, this timescale is driven by the charge-exchange reaction with O_2, while at higher altitudes it is driven by charge-exchange with H_2, the locally dominant species (see Figure 2). The profiles for the transport timescale are similar in the northern and southern polar regions. A peak is seen at approximately 100 km, of the order of 10^2 to 10^3 s. At higher altitudes, the average timescale reaches a stable value of about 100 s for both species. In the equatorial region, the peak occurs approximately at the same altitude as in the polar regions, but the value is at least one order of magnitude higher for both species. At higher altitudes the average is more or less stable between 10 and 100 s. In all regions, the peak at low altitudes originates from a local spike in the ion scale height, corresponding to a plateau in the density profile close to the surface (not shown). At high altitudes, the average transport timescale is lower in the equatorial region as the ions inside the closed field lines move at higher speeds.

For both ions, the chemical lifetime is significantly greater than the transport timescale except very close to the surface (below approximately 200 km), where the number density of O_2 is the largest: there, the two are comparable, as shown in the bottom panels of Figure 6. As a result, very close to the

surface charge-exchange processes with O_2 may be significant. However, by comparing the production rate of O_2^+ from this reaction to that from other ionization sources of O_2 (photoionization and electron impact), we found that the charge-exchange reaction contributes at most to 1% of the total local production rate, hence is a negligible source. We still included the charge-exchange reaction between O_2 and O_2^+/O^+ in our model, and checked that this addition, slowing down O_2^+, has almost no effect on the density map of either ion species.

H_2O^+ was found to react with its neutral parent close to the surface, where densities are highest. The chemical reaction is $H_2O + H_2O^+ \longrightarrow H_3O^+ + OH$, hence H_2O^+ is converted to H_3O^+. However, the latter species was found to be lost mainly through transport, contrarily to what had been assumed by Eviatar et al. (2001), since the chemical loss timescale of recombination with electrons was found to exceed by 3-4 orders of magnitude the transport timescale. As H_2O^+ and H_3O^+ have similar masses, it does not matter which species is simulated, and for this reason we considered H_2O^+ to be collisionless, considering it effectively like a "water ion".

The other ionospheric species are minor components in the ionosphere and their chemical timescale was found to vastly exceed the transport timescale everywhere. In particular, H_2^+ is primarily lost by transport, and its recombination with electrons is negligible everywhere unlike what Cessateur et al. (2012) assumed. Based on our analysis, it is therefore justified to assume all ionospheric species to not undergo any collision or chemical reaction.

3.4.3. No secondary electrons

As shown in Section 3.4.1, the atmosphere is optically thin, so the photo-ionization process is dominated by the lower end of the EUV energy spectrum everywhere in Ganymede's exosphere. The mean energy of the photo-electrons produced is between 6 eV for H_2, 22 eV for O and values in between for H_2O and O_2 at solar minimum conditions (Huebner et al. (1992)). These values are close or below the ionization threshold. Combined by the fact that electron-impact ionization cross-sections are very low below a few tens of eV, the contribution of photo-electrons to the ionization of the exosphere is negligible compared with photo-ionization and has been neglected here.

4. Results

4.1. Overview

Table 3 shows a comparison of the total production, impact and escape rates between the ion species simulated. The total production rate is dominated by O_2^+ as a direct consequence of O_2 dominating in the neutral exosphere. For each ion species, the main production channel is ionization of the parent neutral, except for O^+, which is primarily produced via dissociative ionization of O_2. For H_2^+, H_2O^+, H^+ and OH^+, the majority of ions produced escape from the simulation box, while for O^+ and O_2^+ more than half of the ions produced]impacts Ganymede's surface. This difference is due to the spatial distribution of O_2 in the exosphere: being concentrated mostly close to the surface (see left panel, Figure 2) the oxygen ions, being also created close to the surface, have a better chance of impact compared to, for example, H_2O^+ produced from H_2O which is more spread in altitude

476 (see right panel, Figure 2).

Rate ($\times 10^{23} s^{-1}$)	O_2^+	O^+	H_2^+	H_2O^+	H^+	OH^+
Total production	90.4	12.8	14.7	10.6	3.4	3.1
Impact	73.1	9.9	7.3	2.8	1.1	0.8
Escape	17.3	2.9	7.4	7.8	2.3	2.3
% of escape	19.1	22.7	50.3	73.6	67.6	74.2

Table 3: Comparison between ionospheric species in terms of total production, impact, and escape rates. The escape rate (third row) is derived from the difference between the total production (first row) and surface impact (second row) rates. The bottom line provides the percentage of escaping ions.

477 *4.2. Number density, bulk velocity and temperature maps*

478 We present 2D maps of the number density (Section 4.2.1), bulk veloc-
479 ity (4.2.2) and temperature (Section 4.2.3) in three different planes for O_2^+.
480 Although the values of these quantities differ between ion species, the global
481 structure of the maps and the main features highlighted are similar for all
482 ions, hence only the results for O_2^+ are presented, owing to its dominance in
483 terms of number density.

484 *4.2.1. Number density*

485 Panels a), b) and c) of Figure 7 show the number density of O_2^+ in the
486 XZ, YZ and XY planes, respectively. The density profiles are not symmet-
487 ric around the moon and reproduce the detailed structure of Ganymede's
488 magnetosphere. From these plots we see that the ionospheric plasma is not

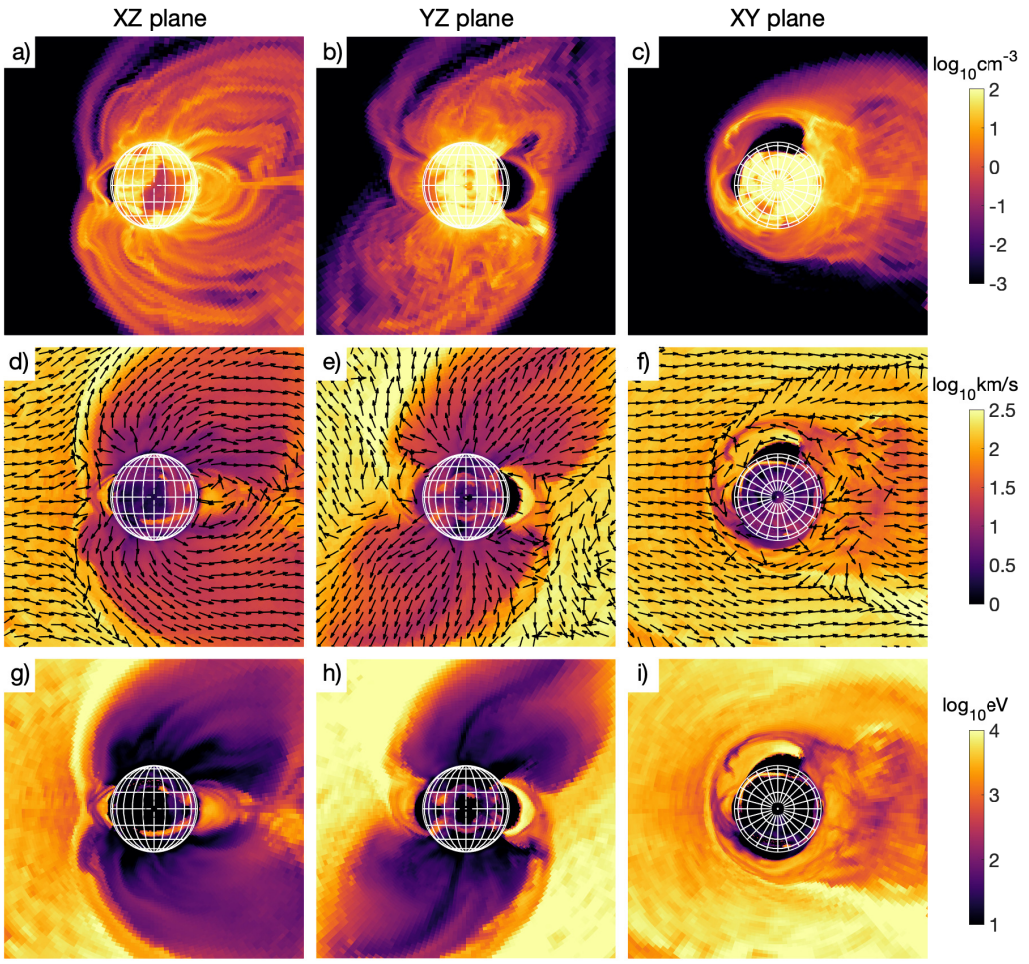

Figure 7: Maps of the distribution moments for O_2^+ with Ganymede at 11 a.m. in Jupiter's solar local time. All color scales are logarithmic. Top row: Number density. Middle row: Bulk velocity. Bottom row: Bulk temperature. For a generic plane "AB", 'A' points to the right and 'B' points up.

spatially confined close to the moon, but extends along the Alfvén wings and in the direction of corotation of the Jovian plasma.

In the XZ and XY planes the Jovian plasma flows from the left to the right of the plot, i.e. the upstream hemisphere is to the left of the moon. In this region, the ionospheric plasma is confined within a distance of approximately 1 R_G from the surface, corresponding to the location of the magnetopause in the hybrid model (see Figure 3).

In all three planes we can distinguish three regions: the first with low density (region I, black colour, $n_{O_2^+} < 10^{-3}$ cm^{-3}), the second with higher density (region II, purple/ dark orange colour, $10^{-3} < n_{O_2^+} < 1$ cm^{-3}) and a region of relatively high density close to the moon (region III, orange/yellow colour, $n_{O_2^+} > 1$ cm^{-3}). In the XZ and YZ planes, the boundary between regions I and II corresponds to the boundary of the Alfvén wings intersecting each plane. Figure 3, showing the magnetic field lines considered in the ionospheric simulation, helps to visualise the projection of the Alfvén wings in these two planes. In the XZ and XY planes, region II extends also in the positive X-direction. This is due to the ionospheric plasma leaving the simulation box in the corotation direction and merging with the Jovian magnetospheric ions. Inside the Alfvén wings the plasma is denser because in this region the electric field is weaker, hence the plasma moves slower compared to outside (see Section 4.2.2). This results with ions accumulating inside the wings.

Region III is found everywhere around the moon, close to the surface. In the equatorial region, the high density extends up to the magnetopause in the orbitally leading hemisphere, as seen in panels a) and c) of Figure 7. The

density in the equatorial region is enhanced by ions which are trapped inside the closed field lines region and perform $\mathbf{E} \times \mathbf{B}$ drift motion around the moon with typical energies of the keV order, hence forming partial radiation belts. The energization of ionospheric ions occurs near the magnetopause boundary in the equatorial region, where strong currents are present resulting from the large curvature of the magnetic field lines. In the XZ and YZ planes, the shape of the mirroring motion along closed magnetic field lines - as illustrated in panels a) and b) - is recognised as the "rounded" curves, reproducing the magnetic field lines, to the left and right of the moon.

There is an asymmetry in the ion density in the YZ plane in the equatorial region between the +Y and -Y hemispheres (Figure 7b), with the number density being significantly lower in the +Y hemisphere. This results from Ganymede's position with respect to the Sun. Since at the time of the G2 flyby the midday longitude (in GPhiO system) was 300°, and the midnight longitude was 120°, the +Y region associated with closed magnetic field lines near the equator is located in the moon's shadow: no ionization of the neutral exosphere occurs in the region of closed magnetic field lines. Therefore, no plasma is generated in this region, resulting in a much reduced density, as shown in Figure 7b.

Panels a) and b) of Figure 7 display some string-like features in the polar regions. These are to be considered as noise in the electric field generated by the hybrid model but which do not compromise the conclusions drawn by our study. The fields were calculated with a resolution of 125 km close to the moon and the noisy patterns suggest that in this region the resolution implemented by the hybrid model might be insufficient for Ganymede's

magnetospheric environment or that in this region there is not enough particle statistics in the hybrid model. In Appendix Appendix A we compare the maps in Figure 7 with those obtained using the MHD model to discern features which are physical from those which are driven by the input fields.

4.2.2. Bulk velocity

Panels d), e) and f) of Figure 7 show the bulk velocity of O_2^+ in the XZ, YZ and XY planes, respectively. As indicated by the arrows, the plasma flows in the direction of corotation and escapes from the magnetosphere either in this direction or through the Alfvén wings. On average, compared to the bulk speed of the Jovian plasma sheet of 140 km/s found outside Ganymede's magnetosphere, the ionospheric plasma moves considerably slower inside Ganymede's magnetosphere and the Alfvén wings, while it moves faster at the Alfvén wings boundaries. For O_2^+, close to the moon the plasma moves on average at 1-10 km/s, while near the wings' boundaries the average speed exceeds 1000 km/s. This difference arises mainly from the large difference in the intensity of the electric field in these two regions. Inside the wings the electric field is significantly weaker compared to that at its boundaries. At the boundaries are found electric currents which, being associated to a strong electric field, accelerate the ions. These currents run all the way along the Jovian magnetic field lines linked to the Alfvén wings and close on one end at Jupiter's ionosphere (Kivelson et al. (2004)) and, on the other end, at Ganymede's magnetosphere.

4.2.3. Temperature

Panels g), h) and i) of Figure 7 show the temperature of O_2^+ in the XZ, YZ and XY planes, respectively. Inside the Alfvén wings the average temperature of O_2^+ (and also of the other simulated species, not shown here) is of the order of 1 eV, but it increases rapidly at the wings' boundaries and the magnetopause regions on the upstream and downstream hemispheres. Note the definition of temperature that is used here: it is related to the variance of the velocity (see Equation 6). A low temperature corresponds to a population of ions which statistically move at speeds close to the bulk speed, while a large temperature indicates that the ions possess a wide range of speeds. For the downstream magnetopause region (at a radial distance of approximately 2 R_G from the surface), the large temperature arises due to the strong magnetopause currents. In this region, there co-exist ions which have been accelerated by currents, hence moving fast, and locally newborn ions which have just been produced and hence move slow. This causes a large variance in the velocity which is reflected in the temperature parameter. A similar argument applies to regions of Ganymede's magnetosphere where electric currents are present, namely the radiation belt (panels g), h) i)), the Alfvén wing boundaries (panels g) and h)) and the upstream and downstream magnetopause regions (panels g) and i)). In these regions, ionospheric ions are accelerated by $\mathbf{E}$ and $\mathbf{B}$ to energies greater than 1 keV.

5. G2 flyby

5.1. Comparison between simulations and Galileo observations

Located above the plasma sheet, the Galileo spacecraft did three flybys of Ganymede: G1 in June 1996, G2 in September 1996 and G29 in December 2000. Unlike other flybys, G1, G2 and G28 were close enough to detect a significant amount of ionospheric plasma according to our simulations. In this section, we compare our simulations to observations from PLS and PWS instruments during the G2 flyby. Closest approach to Ganymede occurred at an altitude of 261 km above the moon's surface in the northern polar region (the closest amongst all flybys). We show results for simulations which were driven by the electric and magnetic fields not only from the hybrid code of Leclercq et al. (2016) (see Section 3.3) but also from the MHD model of Jia et al. (2009). The goal is to check the robustness of our conclusions using different magnetospheric models.

5.1.1. Electron density

Panel a) of Figure 8 shows the electron number density profile along the G2 trajectory as measured by: the PWS instrument (Eviatar et al., 2001) (black curve), an ionospheric simulation driven by fields from the hybrid model of Leclercq et al. (2016) (red curve) and an ionospheric simulation, driven by fields from the MHD model of Jia et al. (2009) (blue curve). The electron number density was obtained by summing the ion density over all ionospheric species, assuming plasma neutrality. The reader is referred to Figure C.13 in Appendix C to visualize the volume mixing ratio of the ionospheric species along the spacecraft trajectory. The green curve shows the

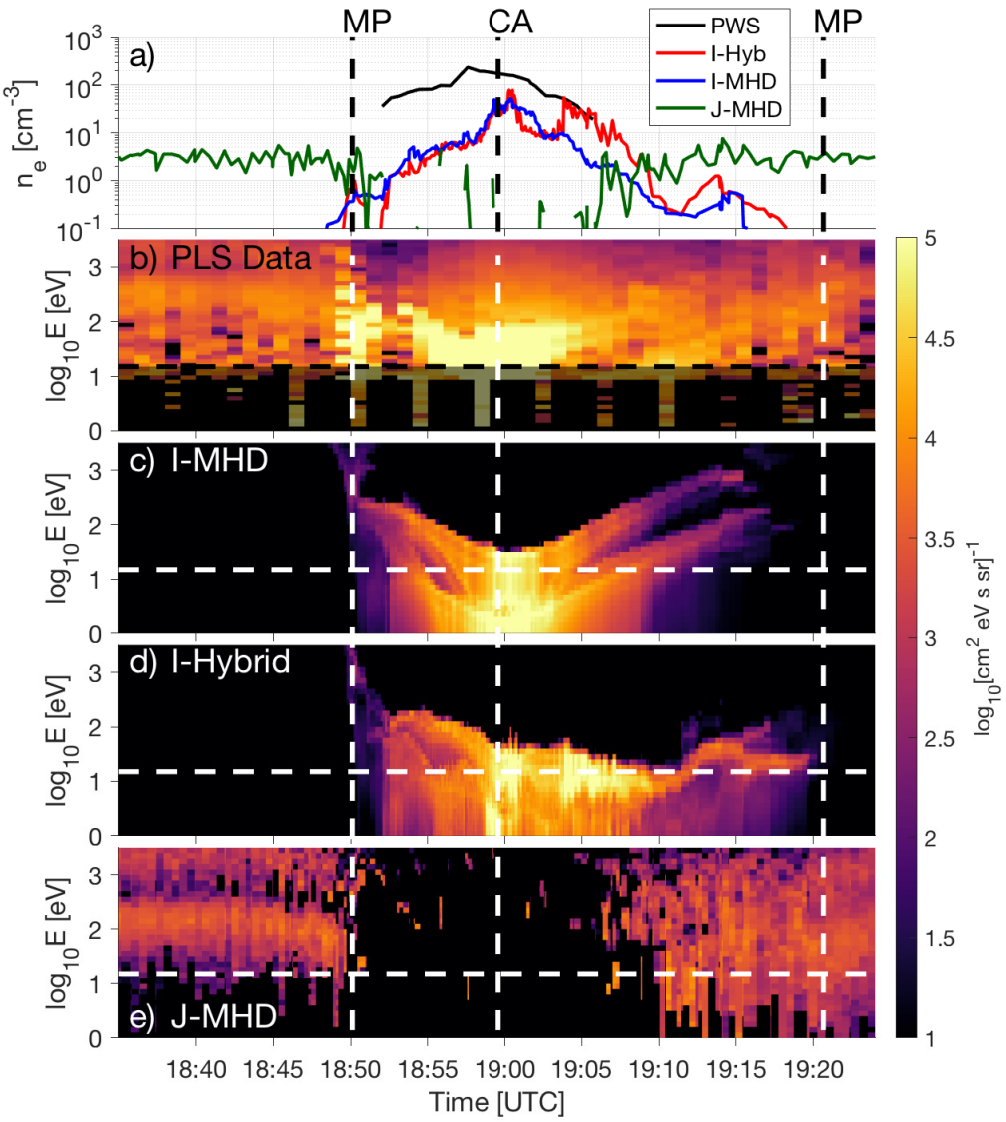

Figure 8: a): Electron density profiles along the G2 trajectory, from: the PWS instrument (black curve) (from Eviatar et al., 2001), the ionospheric simulation using the fields from the hybrid model of Leclercq et al. (2016) ('I-Hyb', red curve) and the ionospheric simulation using the fields from the MHD model of Jia et al. (2009) ('I-MHD', blue curve). The green curve shows the number density of Jovian thermal ions, simulated using the fields from the MHD model ('J-MHD'). b): Energy spectrogram of the total ion intensity (mean over angle) as recorded by the PLS instrument; below 15 eV (shaded region) the processing of the dataset is considered unreliable (see Appendix B regarding data processing from raw data (count/s) to physical units). c-d): Energy spectrograms of the simulated ionospheric ion intensity, in the reference frame of the spacecraft, from simulations which made use of the fields from the MHD model of Jia et al. (2009) (panel c) and the hybrid model of Leclercq et al. (2016) (panel d). e) Energy spectrograms of the simulated thermal Jovian ions intensity, in the reference frame of the spacecraft, from simulations which made use of the fields from the MHD model of Jia et al. (2009). The dashed white horizontal line in panels c-e) represents the energy limit (15 eV) below which the processing of the PLS dataset is considered unreliable. The dashed black/white vertical lines show the time of magnetopause crossings (MP) and of closest approach (CA).

number density of Jovian ions obtained from an ad hoc simulation in which the fields from the MHD model were used. The Jovian magnetospheric ion population was assumed to be constituted of only H^+ and O^+. We ran a simulation where the Jovian test particles were injected in all planes of a simulation box with size 20 R_G × 20 R_G × 20 R_G (in the X, Y and Z directions, respectively) with Ganymede in the center. Test particles were launched assuming a bi-Maxwellian velocity distribution (one in the X-direction and one in the YZ-directions). Both distributions had a temperature of 360 eV (Neubauer (1998)) and were centered at 0 km/s for the YZ-directions and at the corotation velocity of 140 km/s for the X-direction. Plasma composition was assumed to be 87% O^+ and 13% H^+. In order to reproduce the number density of 4 cm^{-3} of the bulk population outside the plasma sheet (Kivelson et al. (2004)), the density of O^+ was set to 3.48 cm^{-3}, and that of H^+ to 0.52 cm^{-3}. Test particles were followed either until they hit the moon or until they crossed any of the boundary planes. A simulation with the same input conditions for the Jovian plasma was performed using the fields from the hybrid model, and the results were confirmed to agree very well with those obtained using the fields from the MHD model.

Before 18:50 UTC and after 19:10 UTC the simulations show that the plasma is primarily of Jovian origin and the modeled electron density agrees very well with previous Voyager and Galileo observations (Kivelson et al., 2004) (see Figure 8a). These time periods correspond to when the spacecraft was located outside Ganymede's magnetosphere: the magnetopause crossing happened at 18:50 UTC inbound and at 19:23 UTC outbound (Kivelson et al., 1997). The Jovian plasma does not gain full access into Ganymede's

magnetosphere in the northern polar region: the plasma number density decreases after the inbound MP, and increases again to its value outside the magnetosphere at the outbound MP. The discontinuity of the green line inside the magnetosphere shows that the Jovian test particles did not cross all the ionospheric cells containing the spacecraft trajectory. The simulations demonstrate that the plasma measured by PWS near CA was primarily of ionospheric origin. Ionospheric ions are observed starting from 18:50 UTC. The density profile increases until closest approach, then decreases in the outbound leg. The density maximum near CA is expected in relation to the higher production rate of ionospheric plasma, associated to the higher density of exospheric species (see Figure 2). Most of the ions crossing the spacecraft trajectory are O_2^+ ions, followed by H_2^+, followed by the other simulated species. The simulated electron density is higher when the fields from the hybrid model are used. This results from the lower electric field derived by the hybrid model, compared to the one obtained in the MHD model of Jia et al. (2009) (see top panel of Figure 4). However, the electron density is consistently underestimated in the simulations, regardless of the electromagnetic fields used as input. When using the fields from both magnetospheric models, the discrepancy between modeled and observed electron density exceeds the order of magnitude and is found to be even higher in the inbound leg of the trajectory, i.e., before 19:00 UTC.

5.1.2. Ion energy distribution

Panels b), c), d) and e) in Figure 8 show the ion intensity plotted on an energy spectrogram as recorded by: the PLS instrument (panel b)), an ionospheric simulation using the fields from the MHD model of Jia et al.

(2009) (panel c)), an ionospheric simulation using the fields from the hybrid model of Leclercq et al. (2016) (panel d)) and a simulation of Jovian ions using the fields from the MHD model. The color scale is logarithmic and the range is indicated in the bar adjacent to the three panels on the right. For panels c) and d), only the contribution from ionospheric ions is shown. Similarly to findings in panel a), energy spectrograms attest that ionospheric ions dominate from the time of the first MP crossing to 19:10 UTC. In the PLS spectrogram (panel b), after 19:10 UTC, a "tail" of plasma (orange/light yellow) emerges from the lower energy limit (15 eV). Its energy increases over time (while the intensity decreases) in a similar fashion to the bulk ion population after 19:02 UTC. Key features of panel b) are seen also in panel c). These include: the relative variation in energy of the ion bulk population over the whole flyby, which follows a remarkably similar trend to the measured values, and the "tail" of plasma after 19:10 UTC. Discrepancies between panels b) and c) concern the overall ion intensity and the ionospheric population energy near CA, which are lower in the simulation. Panel c) exhibits the presence of two ion populations, characterized by two different energies along the flyby via two distinctive tails outbound. The population with higher energy includes heavy ions, such as O_2^+, O^+, H_2O^+, OH^+. The population with lower energy includes light species, i.e. H_2^+ and H^+. The reader is referred to Figure D.14 in Appendix D to visualize the contribution from each individual ionospheric species to the energy spectrum. In panel d), the energy of the ion population over time is found to vary before CA, in a similar way to panels b) and c). However, after CA the ion energies do not exhibit a double tail as seen in the PLS observations (panel b)).

Heavy and light species do not exhibit a dichotomy in the spectrum shown in panel d). The difference between panels c) and d) originates solely in the configuration of **E** and **B** around Ganymede, which fully determines the ion motion according to Equation 3.

We note that for both simulations, the majority of the ion population near CA is found below the energy threshold of the PLS instrument. Most likely, ions were accelerated by a spacecraft potential $V_{S/C}$, and their detection by PLS depended on the sign and strength of $V_{S/C}$. We cannot draw further conclusions on this matter, however, owing to the lack of constraints on the spacecraft potential during the G2 flyby.

In summary, we find that: (1) ionospheric ions dominate within the magnetosphere of Ganymede during the G2 flyby (up to $\sim$ 19:10 UTC); (2) the modeled electron number density is underestimated compared with PWS observations, regardless of the electromagnetic field configuration chosen to solve the equations of motion of the ion species; (3) our simulations driven by the electromagnetic field from the MHD model (Jia et al., 2009), reproduce very well the PLS energy distribution but underestimate the particle intensity.

5.1.3. Ion drift velocities

Taking the moments of order 1 from the ion intensity measured by PLS, we can derive the parallel and perpendicular components of the ion bulk velocities (with respect to the magnetic field) along the trajectory. We have compared the bulk velocity profiles from the simulations driven by the MHD model, with those obtained from PLS during G2 (Frank et al., 1997b). The results of this analysis are shown in Figure 9 for O_2^+ and O^+. Frank et al.

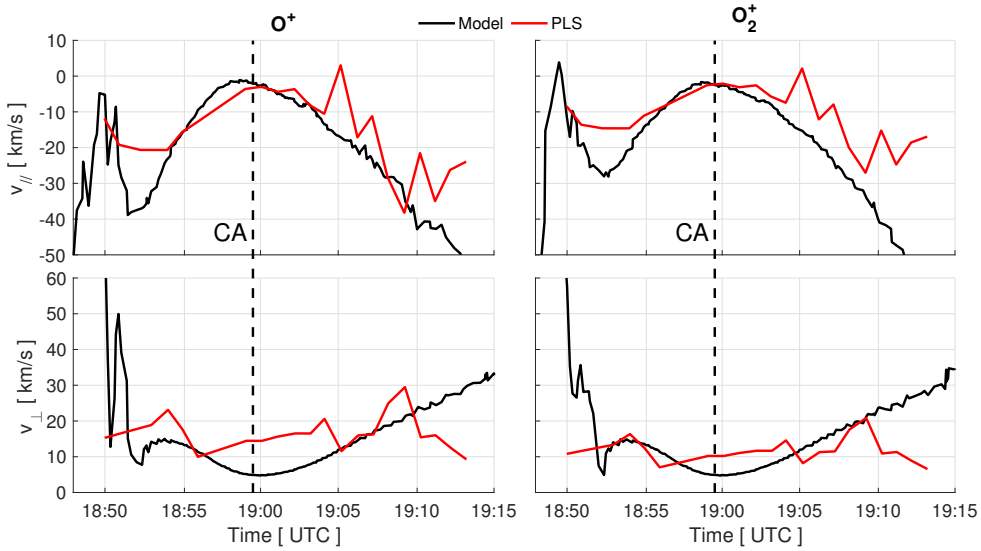

Figure 9: Top: Parallel (with respect to the local magnetic field) bulk velocity component for O^+ (left) and O_2^+ (right) along the G2 trajectory, as obtained from the ionospheric model (black curve) and the PLS instrument (red curve). The PLS profile is originally from Frank et al. (1997b), who assumed only H^+ to calculate the moment, and was adapted to an ionosphere composed purely of O^+ (left panel) or O_2^+ (right panel). Bottom: Same as for the top panels, but for the perpendicular component of the bulk velocity (with respect to the local magnetic field).The modeled results are from simulations driven by the electric and magnetic fields from the MHD model of Jia et al. (2009).

(1997b) assumed the plasma to be composed only of H^+ ions, in an attempt to match the electron number density measured by the PWS instrument for the G1 trajectory (Gurnett et al., 1996). Vasyliūnas and Eviatar (2000) reinterpreted the observed ion flux as being composed of O^+ ions. Besides the difficulties of having mainly H^+ in Ganymede's magnetosphere, their reinterpretation was motivated by the higher electron density measured by PWS at G2 (Eviatar et al., 2001). Using a multi-fluid MHD model of Ganymede's magnetosphere, Paty et al. (2008) provided yet another interpretation of the PLS observations. In their model, they found O^+ to be present with energies below the instrument's threshold. As a result, this ion species would have not been measured by the instrument. In contrast, in their model the energy range of H^+ ions is mostly above the threshold, so they deduced that H^+ was the species that would have been observed by the instrument. Our results differ from those obtained by Paty et al. (2008). In our model, H^+ reaches a maximum energy of about 1 eV near CA (the yellow part at the bottom of panel c) in Figure 8), which is well below the threshold of the PLS instrument, and O^+ reaches approximately 20 eV (the spectrogram shown in panel (c) of Figure 8 incorporates all ionospheric species, so the contribution from each individual species cannot be seen; individual contributions are shown in Appendix D). This trend is opposite to that obtained by Paty et al. (2008), who found H^+ to be above the energy threshold and O^+ below. It is not trivial to explain the difference between the findings of Paty et al. (2008) and our model, considering that the two models are very different in their assumptions and in their approach.

The results of the ionospheric model fully rely on the fields used, and we

note that these come from magnetospheric models which were quite different in nature compared to the MHD model of Paty et al. (2008). For starters, the MHD model of Jia et al. (2009) is single-fluid (O^+), while that of Paty et al. (2008) is multi-fluid (O^+ and H^+). The former calculates the fields on a spherical grid with very high resolution close to the surface (down to 26 km), while the latter implements a Cartesian grid with the highest resolution being about 120 km close to the moon. The plasma properties at the ionospheric boundary are also different between the two models: Jia et al. (2009) used a density of 550 amu/cm^3, while Paty et al. (2008) set this parameter to 5200 amu/cm^3 with a ratio of 4:1 between O^+ and H^+. Furthermore, Paty et al. (2008) did not include ionospheric species other than H^+ and O^+ and thus, could not model and/or comment on the contribution of other species (i.e., O_2^+, etc.) which are considered in the present work. Hence, it is not surprising that the findings from the ionospheric model differ from those from the MHD model of Paty et al. (2008).

According to our model, the majority of ions observed by PLS were O_2^+ ions (see Appendix C), which populate the higher energy portion of the spectrogram. In Figure 9, we show the comparison for the velocity components only for O^+ and O_2^+ as these two species were found to provide the best agreement with PLS observations, which were adapted to assume only a single ion species, either O^+ (left panel) or O_2^+ (right panel). Near CA, O_2^+ seems to provide the best agreement between observations and simulations, while after CA O^+ (and other species similar in mass, such as H_2O^+ and OH^+ [not shown]) seems more suitable. Note, however, that the comparison is limited as no error bars were provided for the observed drift velocities.

We also note that the model reproduces better the parallel component of the plasma velocity than the perpendicular component. In particular, near CA the ionospheric model underestimates the perpendicular component by a factor of 2, for a pure O_2^+ ionosphere (bottom, right panel in Figure 9), and by a factor of 3, for a pure O^+ ionosphere (bottom, left panel in Figure 9). These comparisons suggest that from 18:55 UTC till around CA approach the plasma observed by the PLS instrument was O_2^+ (or a mixture of O^+ and O_2^+, which provides an equally good fit [not shown]), while after CA it was most probably a mixture of O_2^+, O^+ and lighter ionospheric species, such as H_2^+, which is dominating at high altitudes.

To understand further the discrepancy in the perpendicular component near CA between PLS data and the simulations, we have compared the Cartesian components of the velocity. We have used the profiles from Frank et al. (1997b) and adapted them assuming a pure O_2^+ ionosphere, instead of H^+, as the former species is not only the dominant one found in the model, but also seems to give the best agreement with the observations. The results are shown in Figure 10 for the time of flyby near CA. During this period, the spacecraft was flying less than 1000 km above the moon's surface, making its closest approach at 261 km. PLS observed ionospheric ions to move at slow speed in the corotation direction (positive X), and in the anti-Jovian direction (negative Y). At closest approach the mean velocity in the Z-direction was 0 km/s, meaning that the ions were observed to move purely in the positive X and negative Y direction. Comparing the PLS profiles with those obtained from our model in Figure 10 suggests that the discrepancy in the velocity comes mainly from the negative Y component. In the model, the ions move

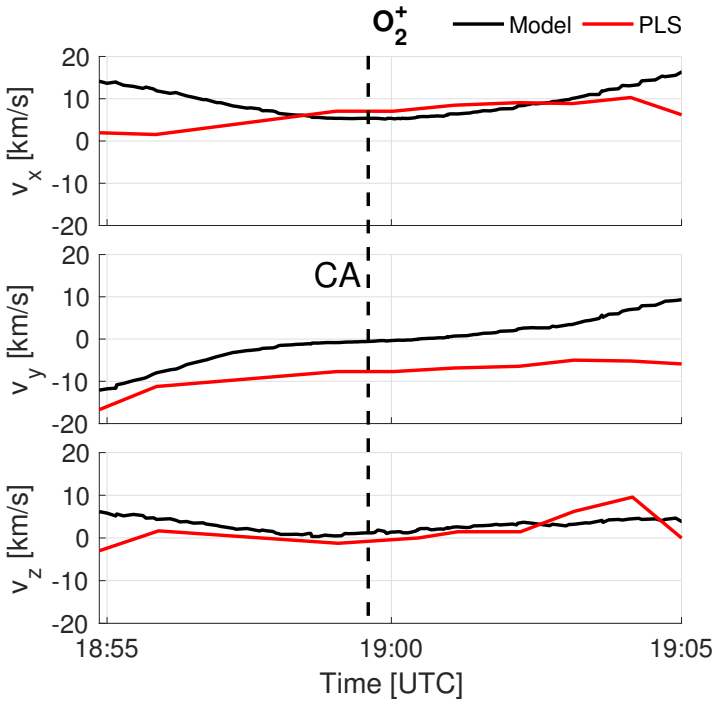

Figure 10: Cartesian components of the mean O_2^+ velocity as found by our model (black curve) and the PLS instrument (red curve), assuming the latter recorded only this ion species.

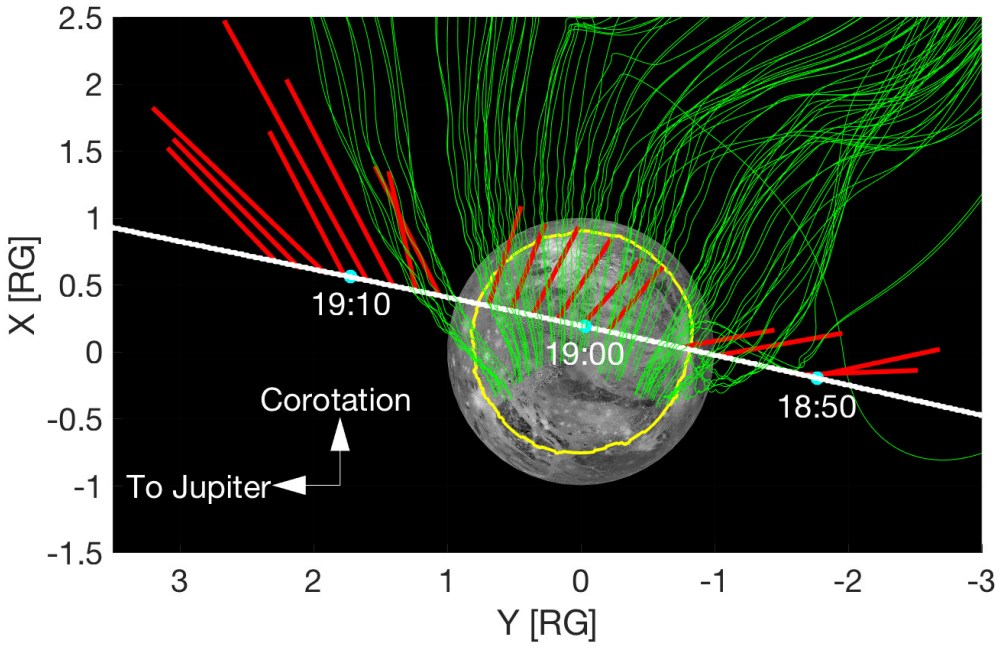

Figure 11: White, bold line: Trajectory of the spacecraft for the G2 flyby. Red lines: Bulk velocity vectors as observed by the PLS instrument (Frank et al., 1997b). Green curves: Selection of O_2^+ test particle trajectories which intersect the path of the spacecraft. Yellow circular line: Northern boundary between open and close magnetic field lines.

only in the positive X direction, and do not drift in the anti-Jovian direction. Figure 11 helps to visualize this finding. Superposed along the spacecraft trajectory are the mean velocity vectors derived by PLS (Frank et al., 1997b) (red lines), and a selection of O_2^+ test particle trajectories which cross the spacecraft trajectory (green curves). By inspection of Figures 9 and 10 we conclude that the perpendicular component missing in the simulations is determined by an ion flow in the anti-Jovian (negative Y) hemisphere which is absent in the ionospheric model.

5.2. Discussion on the model-observations comparison for G2

The ionospheric model underestimates the electron density irrespective of the fields used to run the simulation (see Section 5.1.1). This discrepancy is highest in the inbound leg of the flyby. For the simulation which uses the fields from Jia et al. (2009), the discrepancy is approximately a factor of 30 at 18:52 UTC and progressively reduces to a factor of 5 near CA. The same simulation provides, however, a very good agreement with observations in terms of the ion energy distribution (see Section 5.1.2). Therefore, the fields from this model seem to provide an accurate description of the field configuration during the G2 flyby and not to be responsible for the underestimation of the number density. To explain the discrepancy in the ionospheric number density between our model and the observations, two concrete possibilities are therefore left:

- The underestimation of the ionization frequency;
- The underestimation of the number density of exospheric species.

Photo-ionization depends on the photo-ionization cross-sections, which are well known within 15%, and on the solar flux which should be known within a factor of 2 or less. Hence, uncertainty on photo-ionization cannot be the main reason for the discrepancy in the electron number density. For reference, over the solar cycle, the ion production rates increase by less than a factor of 2. The ionization process from the impact of energetic Jovian electrons is less-constrained as we do not know the energy and spatial distribution of this population inside Ganymede's magnetosphere. In our model, the ionization frequency is assumed to be constant everywhere in the region

of open magnetic field lines. This is likely not the case, as suggested by the non-uniform location of aurora reported by McGrath et al. (2013) and Molyneux et al. (2018). However, it is very unlikely that the flux of energetic Jovian electrons is 10 times higher or more compared to what we assumed in our model. If else, the flux of these electrons - constrained by Galileo observations outside Ganymede's magnetosphere - should be reduced inside. We conclude that an underestimation of the density of exospheric species is most likely the reason for the low ion densities provided by the ionospheric model . Leblanc et al. (2017) fine-tuned the surface sputtering rate in order to match the column density of O_2 estimated by Hall et al. (1998). As a result, they obtained an exosphere which is dominated by O_2 near the surface, with a mean density of 5×10^7 cm^{-3}. Hall et al. (1998) derived the column density by combining three observational constraints: the aurora brightness measured by the Hubble Space Telescope, the electron density measured by PWS along the G1 trajectory and the upper limit on the far-UV absorption optical depth derived by the UV Spectrometer of the Voyager spacecraft during a stellar occultation event (Broadfoot et al. (1979)). By combining this set of observational constraints, Hall et al. (1998) assumed not only that there is no time variation, but also that the section of exosphere which was studied during the stellar occultation in 1979 was the same, in terms of density, as that found in the region where aurorae are generated. However, all models of Ganymede's exosphere suggest that the distribution of exospheric species is not uniform across the surface due to the sources of production (sublimation and ion sputtering), which do not occur uniformly on the surface. In addition, most of the electron population measured by PWS during G1 and

G2 is of ionospheric origin. Hence, a large part of these electrons may not be energetic enough to excite auroral emissions. We argue that the source of energetic electrons at the origin of aurora comes from the Jovian magnetosphere, and that therefore the electron densities used in Hall et al. (1998) to estimate the oxygen abundance are overestimated. The aurora brightness is proportional to, amongst other parameters, the energetic electron flux and the neutral density. Therefore, the same aurora observed by HST can be matched by decreasing the electron flux and increasing the molecular oxygen density. Further simulations of the exosphere are needed in order to make a more quantitative statement on how much the exospheric density needs to be increased. Furthermore, being indirectly related to the same production process, an increase in the density of O_2 would imply an increase in the density of H and H_2 in the exosphere. This could bring the H Lyman-α brightness calculated with the model of Leblanc et al. (2017) in line with that observed by the UV spectrometer on board the Galileo spacecraft, while currently the brightness in the model is underestimating the observations by more than one order of magnitude.

We calculated that by boosting by a factor of approximately 10 the column densities of all species, and still assuming a constant electron-impact ionization frequency in the polar regions, the derived ionospheric number densities match the observations along the Galileo G2 trajectory. This results in an O_2 column density around 3×10^{15} cm^{-2}, which is slightly above the upper limit estimated by Hall et al. (1998), but most likely within the error bars.

In terms of energy distribution, our simulation results are sensitive to the

electromagnetic field configuration used to run the simulation (see panels c) and d), Figure 8). To assess the sensitivity of the results to the spatial resolution of the electric and magnetic fields, we ran two simulations using the fields from the MHD model of Jia et al. (2009): one with a spatial resolution for the fields of 0.1 $R_G \equiv 263.41$ km (low resolution), and one with a resolution of 0.05 $R_G \equiv 131.7$ km (high resolution). The resulting maps are very similar between the two simulations (not shown), indicating that the resolution does not affect significantly the outcome of the simulations. In panel c) of Figure 8, the spectrogram shows results from a simulation driven by fields with high resolution. The spectrogram generated by the simulation with low resolution looks similar, and all the key features, also seen in the observed spectrum (panel b), Figure 8) are also present. For the electron density along the G2 trajectory, the resulting profiles are similar when using the low and high resolution fields of the MHD model. The higher resolution fields lead to a slightly increased density near CA, but not enough to justify the discrepancy with the values derived from PWS measurements.

By comparing Figures 9 and 10 in Section 5.1.3, we associated the discrepancy, between our model and PLS observations, in the perpendicular drift velocity near CA with a flow in the negative Y direction. This flow was observed by PLS during the flyby but not reproduced by our model. This perpendicular flow indicates that cross-field currents flow in Ganymede's polar ionosphere, suggesting that there is enough resistivity provided by the neutral species. These currents show that the ionosphere is not spatially homogeneous. The hybrid model of Leclercq et al. (2016) and the MHD model of Jia et al. (2009) both assumed a spherically symmetric ionosphere due to

the current lack of knowledge on the spatial distribution of the ionospheric plasma. As a result, these currents, being generated by an asymmetry in the spatial distribution, are not reproduced in the magnetospheric models. A current flowing from the Jupiter-facing (positive Y) to the anti-Jupiter (negative Y) hemisphere suggests that the production of plasma is more intense in the Jovian-facing hemisphere, and the charge disparity between the two hemispheres sets up a potential difference which induces a Pedersen current. This asymmetry in the production rate can be explained by a denser exosphere in the Jovian-facing hemisphere or by a stronger flux of magnetospheric electrons which are able to ionize the neutral exosphere. Leblanc et al. (2017) found that for the G2 epoch the O_2 density was highest in the Jupiter-facing hemisphere, which supports our argument. Another possibility to explain a denser exosphere in one hemisphere is to have a more intense, in terms of flux or energy, sputtering process by Jovian magnetospheric ions. In this picture, the flux of magnetospheric electrons would be enhanced, leading to a higher production rate of ionospheric plasma. This process is currently being investigated, but beyond the scope of the present study. Moreover, this argument provides an explanation for the enhanced brightness of aurora emissions in the Jovian-facing hemisphere observed by HST and reported in McGrath et al. (2013) and Molyneux et al. (2018) .

6. Conclusions

We have presented the first three-dimensional model of Ganymede's ionosphere, assuming a background configuration of the moon corresponding to that during the G2 flyby. We found that O_2^+ is the most abundant species,

followed by O^+, H_2^+ and H_2O^+, despite finding the first two species mainly impacting the moon's surface. For other species, the majority of the population escapes the magnetosphere through the Alfvén wings or in the direction of corotation of the Jovian plasma. The dominance of O_2^+ and O^+ ions as source of surface impact is related to the distribution of O_2, which is concentrated very close to the surface, unlike for other neutral species. We found that the ion outflow velocities measured by PLS during G2 (Frank et al., 1997b) are most consistent with O_2^+ ions escaping Ganymede's magnetosphere in the direction of corotation. This differs from the interpretation of Frank et al. (1997b), who assumed H^+ to be the only species, from the interpretation of Vasyliūnas and Eviatar (2000), who reinterpreted the PLS data as being an outflow of O^+, and from that of Paty et al. (2008) who found both species to be present in the ionosphere, but H^+ to be the only one detected by the PLS instrument.

By comparing the results from our model with the electron density profiles recorded by PWS and the ion energy spectrogram recorded by PLS, we confirmed the ionospheric nature of the plasma starting from the inbound magnetopause crossing, until approximately 19:10 UTC. We also obtained a very good agreement with the ion energy distribution measured by the PLS instrument when using the fields derived by the MHD model of Jia et al. (2009) as input. However, our simulation predicts lower intensities overall and lower energies near closest approach, interpreted as a velocity in the negative Y direction which is not reproduced in our model. This "missing current" from positive to negative Y may be explained by considering that the magnetospheric models considered in this work implemented a spatially constant

and temporally uniform ionosphere, which prevent non-uniform distributions to form. A non-uniform distribution would set up a potential difference which in turn would induce cross-field currents, assuming a resistivity high enough to sustain this current, which is provided by the neutral atmosphere. The cross-field motion observed by PLS indicates that the ionosphere is not uniform, and suggests that the plasma production rate might be higher in the Jovian-facing hemisphere. This could be explained by an increased flux of magnetospheric plasma, which boosts the surface sputtering (and so the density of neutral species) and the ion production through electron impact, or by an increased exospheric density related to the accumulation of O_2 in the Jovian-facing hemisphere, as found by the exospheric model of Leblanc et al. (2017).

The discrepancy between our simulations and the values obtained by PWS in terms of the electron number density is likely to be caused primarily by an underestimation of the exospheric densities (see Section 5.2). We estimated that the density of O_2 should be approximately a factor of 10 higher (in terms of column density) in order to match the observations from PWS. This would reduce the ions mean free path, and potentially require the inclusion of collisions close to the surface. Furthermore, we would have to assess if energetic electrons undergo any significant energy degradation close to the surface. However, we have checked that the exosphere remains optically thin to EUV radiation (assuming a boosted exosphere). The results of our model suggest that in order to improve further the comparison with Galileo data from the G2 flyby, magnetospheric models should take into account the asymmetries in the ionosphere, which are generated by the spatially non-

uniform production mechanisms and the non-uniform exosphere. Ultimately, a self-consistently coupled model of the ionosphere and magnetosphere should address that.

Based on the outcome of the comparison between the model output and observations, the exospheric density profiles seem to be underestimated. In the future we plan to implement a physically suitable modification to the exospheric configuration that would reconcile modeled and observed ionospheric densities. This would help to fully validate the model against Galileo plasma observations and confirm the usefulness and relevance of our model in preparation to the JUICE mission, especially for the Ganymede phase when the spacecraft will be in orbit around the magnetized moon. For example, the 3D electron density distribution could be thus used to select the optimal operating modes of the Radio Plasma Wave Instrument (RPWI). In addition, the density and velocity maps for different ions could be not only directly relevant to the instrument teams, but also used as inputs for spacecraft simulations to calculate quantities, such as the radiation dose received by the spacecraft inside Ganymede's magnetosphere. Furthermore, we plan to assess the surface sputtering rate due to ionospheric plasma precipitation and compare these with the contribution from Jovian ions. These results could be implemented in exospheric models to include the ionospheric source of neutral species in the exosphere. Moreover, our model allows to calculate the production rate and density map of Energetic Neutral Atoms (ENAs) by charge-exchange between ions and neutral species. This could be relevant to the Particle Environment Package (PEP) instrument which will assess the properties and distribution of these particles around Ganymede. Finally,

a self-consistently coupled ionosphere-magnetosphere model could be highly critical for the interpretation of the magnetic field data measured by J-MAG in the moon's environment.

7. Acknowledgements

Work at Imperial College London was supported by STFC of UK through a postgraduate studentship and under grants ST/K001051/1 and ST/N000692/1. FL and RM acknowledge the support by the ANR HELIOSARES (ANR-09-BLAN-0223), ANR MARMITE-CNRS (ANR-13-BS05-0012-02) and by the "Système Solaire" program of the French Space Agency CNES. XJ acknowledges support by NASA's Solar System Workings program through grant NNX15AH28G. Authors also warmly acknowledge the support of the IPSL data centre CICLAD for providing access to their computing resources. We are grateful to Isabella Söldner-Rembold and Roman Chudzinski for their help in combining photo-ionisation cross section sets. We are very grateful to Markus Fraenz for providing the CCATI software (http://www2.mps.mpg.de/projects/mars-express/aspera/ccati/) and offering valuable advice on the PLS data processing. We also wish to acknowledge NASA's Planetary Data System (https://pds.nasa.gov/), through which the PLS raw and calibration data has been made available. We are also grateful to the TIMED/SEE team for providing us with the solar flux data set (http://lasp.colorado.edu/see/).

Appendix A. Identifying input-driven features in the 2-D maps of number density, bulk velocity and temperature

Figure 7 shows 2-D maps of the number density, bulk velocity and temperature for O_2^+ obtained using, as input, the electromagnetic field from the hybrid model of Leclercq et al. (2016) (hereafter referred as 'HYB16'). Figure A.12 shows the same maps obtained using the electromagnetic field from the MHD model of Jia et al. (2009) (hereafter referred as 'MHD09').

Many results discussed in Sections 4.2.1– 4.2.3 apply also for the results obtained using the MHD model. These include: (1) the plasma confined mainly within the Alfvén wings and the closed magnetic field lines, (2) the escape through the wings and the corotation direction at low latitudes, (3) the low velocity/temperature inside the wings, and the high velocity/temperature at the wings' boundaries and in the equatorial region. Overall, implementing either of the two sets of fields leads to the same global convection pattern of the ionospheric plasma and the same order of magnitude for all the first ion moments shown in Figure 7 and A.12.

The differences between HYB16 and MHD09 concern primarily small scale features. For example, the 'string-like' features that appear in HYB16 in the polar regions are absent in MHD09. As explained in Section 4.2.1, these are to be considered as noise in the electric field generated by the hybrid model in relation to the limited resolution of the grid close to the surface, which does not appear to be sufficiently refined to physically resolve the field configuration. Another difference concerns the asymmetry in the YZ plane in the bulk velocity and temperature. For MHD09, velocities are higher in the anti-Jovian hemisphere at low latitudes, while for HYB16 this

is not the case (except close to the surface where speeds are small in both hemispheres). Furthermore, for HYB16 there is no preferential drift in the clockwise direction like there is when using the MHD model, which can be seen also from the less defined arrow directions in panel f) of Figure 7 compared with panel f) in Figure A.12. Finally, in MHD09 the plasma in the polar regions appears to feel a greater pressure in the corotation direction, which limits the upward spread of plasma along the Alfvén wings. In other words, the plasma close to the surface in the polar regions in MHD09 is seen to flow predominantly in the x-direction, contrarily to HYB16, in which the plasma is seen to spread more in altitude. A comparative study to interpret these difference is worth undertaking, but beyond the scope of this work.

Either set of input fields leads to the same conclusions presented in this manuscript, which supports their validity.

Appendix B. Processing of PLS data

Here we describe how the PLS data shown in panel b) of Figure 8 has been processed. PLS is an ion and electron particle detector, which is part of the Galileo instrumentation (Frank et al. (1992)). In this work only the ion data collected by PLS is of importance. PLS consists of seven detectors, each of which detects particles coming from different parts of the sky. They are oriented in such a way that during approximately one spin ($\sim$20 s) of the Galileo spacecraft the whole sky is scanned. In addition to scanning over directions, each PLS detector also scans over energy-per-unit charge (E/Q), from 0.9 eV to 52 keV.

Due to the malfunction of Galileo's main antenna the data rate was very

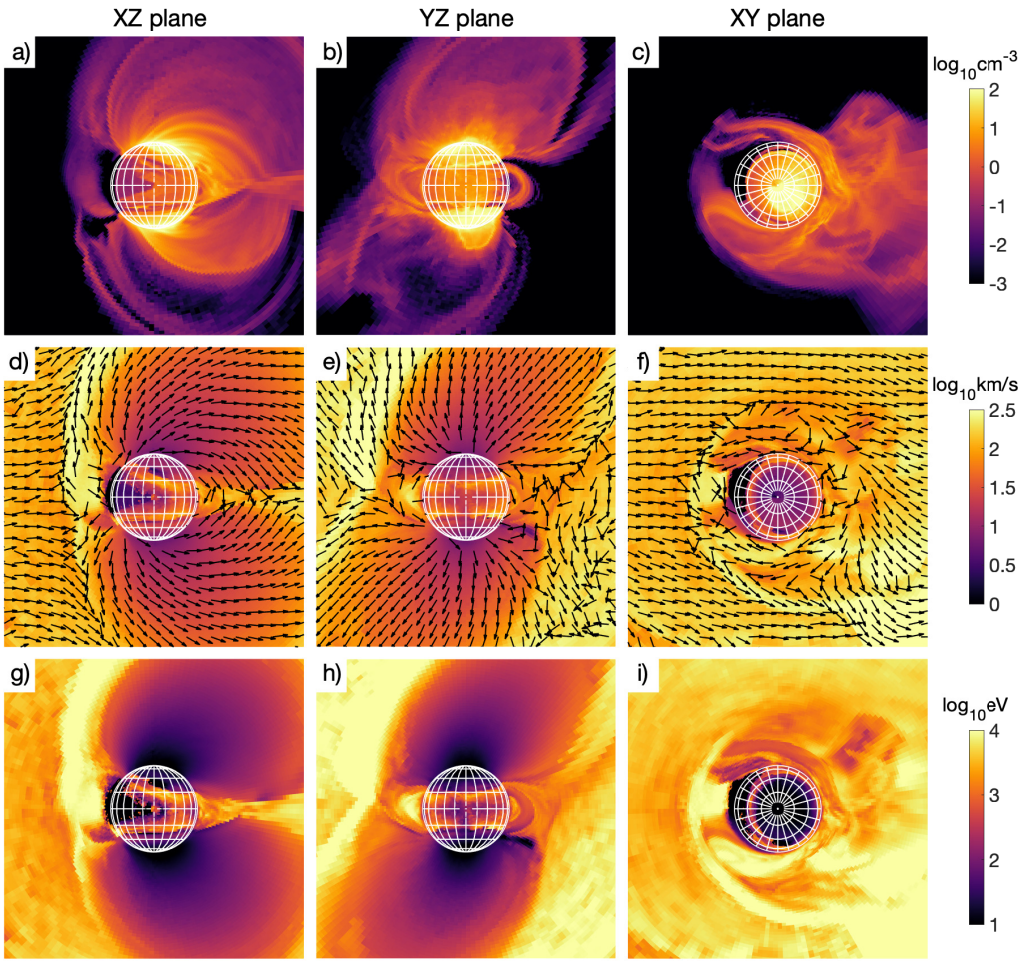

Figure A.12: Maps of the distribution moments for O_2^+ with Ganymede at 11 a.m. in Jupiter's solar local time. All color scales are logarithmic. Top row: Number density. Middle row: Bulk velocity. Bottom row: Bulk temperature. For a generic plane "AB", 'A' points to the right and 'B' points up.

limited during the whole mission. Hence, for each spin only a limited part of the data was transmitted, resulting in an incomplete coverage of the sky in both energy and direction. Additionally, the PLS instrument was also affected by penetrating electrons that entered the detector through the shielding and created noise.

The PLS data shown in Figure 8 has been processed in several steps to compensate for the poor coverage in time, energy and background noise. The processing of the data was done using the CCATI software, originally developed by Markus Fraenz (http://www2.mps.mpg.de/projects/mars-express/aspera/ccati/). First, the raw PLS data was obtained from NASA's Planetary Data System (PDS), in units of counts per second. Every data point has a tag representing the time, energy bin detector number and sector number. The latter represents the spin angle at which the measurement was made. Next, data values for one detector, for which the current, previous and next time steps that have the same energy tag, but a different sector number, are averaged. Subsequently, for each time step a cubic spline interpolation is applied to fill in the empty energy bins. After that, the noise is removed as follows. For each time step, the average and the standard deviation are extracted from the count rate in the energy bins of the four highest energy bins that have non-zero values. The standard deviation, multiplied by 0.2, is added to this average. The result is then subtracted from all energy bins of the corresponding time step, to remove the background noise. This is comparable to earlier PLS studies, which have also used the count rate in the highest energy bins to estimate the background noise [Frank and Paterson (1999); Paterson et al. (1999)]. Next, the data units are converted from counts/s to intensity (also

called differential flux) in $cm^{-2}s^{-1}sr^{-1}eV^{-1}$. This is done by multiplying the data with the 'chi-factor' . The chi-factor was obtained by the PLS team from calibration experiments in laboratory and provided to the PDS. As a final step, averaging in time is performed together with averaging over the seven detectors. This is done using 'box car' averaging, meaning that the time frame is first divided in equally sized bins. Then all the values in each energy-time bin (taken from all the detectors) are summed up and this sum is divided by the number of values in the energy-time bin. Here averaging is done over bins of 60 seconds in length.

The data obtained during the G2 flyby has been obtained with two different scanning modes: one below 15 eV and one above 15 eV. Because of uncertainties in the processing of the data of the low energy scans we only consider the processed data above 15 eV to be reliable.

Appendix C. Volume mixing ratio along G2 flyby

We report in Figure C.13 the volume mixing ratio of ionospheric species calculated along the G2 flyby from a simulation with input electric and magnetic fields from the MHD model of Jia et al. (2009). O_2^+ dominates amongst the ionospheric species from around 18:37 UTC to 19:14 UTC (except for a very short period around 10:08 UTC). The semi-transparent red box from 18:50 UTC to 19:13 UTC indicates the time range from which Frank et al. (1997a) calculated the second moment of the plasma distribution measured by the PLS instrument. Within this time range, our simulation finds that O_2^+ is the dominant species, followed by H_2^+.

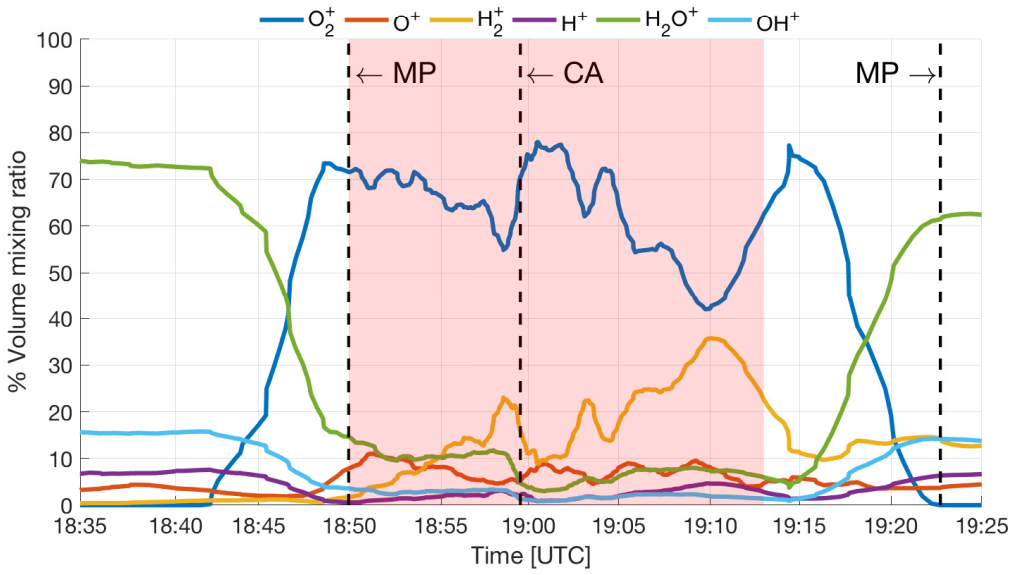

Figure C.13: Volume mixing ratio of ionospheric species calculated along the G2 flyby. The black dashed vertical lines indicate the crossing times of the magnetopause (MP) and closest approach (CA). The semi-transparent red box indicates the time range from which Frank et al. (1997a) calculated the first moment of the plasma distribution measured by the PLS instrument.

Appendix D. Energy spectrum decomposition

We report in Figure D.14 the energy spectrum along the G2 flyby from: the PLS instrument (panel a), the ionospheric model considering all ionospheric species (panel b) and the ionospheric model separating the contribution from each different ionospheric species (panels c-h). The input electric and magnetic fields were taken from the MHD model of Jia et al. (2009).

References

Avakyan, S. V., e. (Ed.), 1998. Collision processes and excitation of UV

emission from planetary atmospheric gases : a handbook of cross sections.

Backx, C., Wight, G.R., Van der Wiel, M.J., 1976. Oscillator strengths (10-70 eV) for absorption, ionization and dissociation in H_2, HD and D_2, obtained by an electron-ion coincidence method. Journal of Physics B Atomic Molecular Physics 9, 315–331. doi:10.1088/0022-3700/9/2/018.

Banks, P., 1966. Collision frequencies and energy transfer. Ions. Planetary Space Science 14, 1105–1122. doi:10.1016/0032-0633(66)90025-0.

Barth, C.A., Hord, C.W., Stewart, A.I.F., Pryor, W.R., Simmons, K.E., McClintock, W.E., Ajello, J.M., Naviaux, K.L., Aiello, J.J., 1997. Galileo ultraviolet spectrometer observations of atomic hydrogen in the atmosphere at Ganymede. Geophysical Research Letters 24, 2147. doi:10.1029/97GL01927.

Boris, J.P., 1970. Relativistic plasma simulation - optimization of a hybrid code. Proc. 4th Conf. on Numerical Simulation of Plasmas (Washington, DC) , 3–67.

Brion, C.E., Tan, K.H., van der Wiel, M.J., van der Leeuw, P.E., 1979. Dipole oscillator strengths for the photoabsorption, photoionization and fragmentation of molecular oxygen. Journal of Electron Spectroscopy and Related Phenomena 17, 101–119.

Broadfoot, A.L., Belton, M.J., Takacs, P.Z., Sandel, B.R., Shemansky, D.E., Holberg, J.B., Ajello, J.M., Moos, H.W., Atreya, S.K., Donahue, T.M., Bertaux, J.L., Blamont, J.E., Strobel, D.F., McConnell, J.C., Goody,

R., Dalgarno, A., McElroy, M.B., 1979. Extreme ultraviolet observations from Voyager 1 encounter with Jupiter. Science 204, 979–982. doi:10.1126/science.204.4396.979.

Cessateur, G., Lilensten, J., Barthélémy, M., Dudok de Wit, T., Simon Wedlund, C., Gronoff, G., Ménager, H., Kretzschmar, M., 2012. Photoabsorption in Ganymede's atmosphere. Icarus 218, 308–319. doi:10.1016/j.icarus.2011.11.025.

Cooper, J.F., Johnson, R.E., Mauk, B.H., Garrett, H.B., Gehrels, N., 2001. Energetic Ion and Electron Irradiation of the Icy Galilean Satellites. Icarus 149, 133–159. doi:10.1006/icar.2000.6498.

Cui, J., Galand, M., Coates, A.J., Zhang, T.L., Müller-Wodarg, I.C.F., 2011. Suprathermal electron spectra in the Venus ionosphere. Journal of Geophysical Research (Space Physics) 116, A04321. doi:10.1029/2010JA016153.

Eviatar, A., Vasyliūnas, V.M., Gurnett, D.A., 2001. The ionosphere of Ganymede. Planetary and Space Science 49, 327–336. doi:10.1016/S0032-0633(00)00154-9.

Feldman, P.D., McGrath, M.A., Strobel, D.F., Moos, H.W., Retherford, K.D., Wolven, B.C., 2000. HST/STIS Ultraviolet Imaging of Polar Aurora on Ganymede. The Astrophysical Journal 535, 1085–1090. doi:10.1086/308889.

Frank, L.A., Ackerson, K.L., Lee, J.A., English, M.R., Pickett, G.L., 1992. The plasma instrumentation for the Galileo Mission. Space Science Reviews 60, 283–304. doi:10.1007/BF00216858.

Frank, L.A., Paterson, W.R., 1999. Intense electron beams observed at Io with the Galileo spacecraft. Journal of Geophysical Research 104, 28657–28670. doi:10.1029/1999JA900402.

Frank, L.A., Paterson, W.R., Ackerson, K.L., Bolton, S.J., 1997a. Low-energy electron measurements at Ganymede with the Galileo spacecraft: Probes of the magnetic topology. Geophysical Research Letters 24, 2159. doi:10.1029/97GL01632.

Frank, L.A., Paterson, W.R., Ackerson, K.L., Bolton, S.J., 1997b. Outflow of hydrogen ions from Ganymede. Geophysical Research Letters 24, 2151. doi:10.1029/97GL01744.

Galand, M., Moore, L., Charnay, B., Mueller-Wodarg, I., Mendillo, M., 2009. Solar primary and secondary ionization at Saturn. Journal of Geophysical Research (Space Physics) 114, A06313. doi:10.1029/2008JA013981.

Grasset, O., Dougherty, M.K., Coustenis, A., Bunce, E.J., Erd, C., Titov, D., Blanc, M., Coates, A., Drossart, P., Fletcher, L.N., Hussmann, H., Jaumann, R., Krupp, N., Lebreton, J.P., Prieto-Ballesteros, O., Tortora, P., Tosi, F., Van Hoolst, T., 2013. JUpiter ICy moons Explorer (JUICE): An ESA mission to orbit Ganymede and to characterise the Jupiter system. Planetary and Space Science 78, 1–21. doi:10.1016/j.pss.2012.12.002.

Gurnett, D.A., Kurth, W.S., Roux, A., Bolton, S.J., Kennel, C.F., 1996. Evidence for a magnetosphere at Ganymede from plasma-wave observations by the Galileo spacecraft. Nature 384, 535–537. doi:10.1038/384535a0.

Hall, D.T., Feldman, P.D., McGrath, M.A., Strobel, D.F., 1998. The Far-Ultraviolet Oxygen Airglow of Europa and Ganymede. The Astrophysical Journal 499, 475–481. doi:10.1086/305604.

Huebner, W.F., Keady, J.J., Lyon, S.P., 1992. Solar photo rates for planetary atmospheres and atmospheric pollutants. Astrophysics and Space Science 195, 1–289. doi:10.1007/BF00644558.

Huebner, W.F., Mukherjee, J., 2015. Photoionization and photodissociation rates in solar and blackbody radiation fields. Planetary and Space Science 106, 11–45. doi:10.1016/j.pss.2014.11.022.

Ip, W.H., Kopp, A., 2002. Resistive MHD simulations of Ganymede's magnetosphere 2. Birkeland currents and particle energetics. Journal of Geophysical Research (Space Physics) 107, 1491. doi:10.1029/2001JA005072.

Itikawa, Y., Mason, N., 2005. Cross Sections for Electron Collisions with Water Molecules. Journal of Physical and Chemical Reference Data 34, 1–22. doi:10.1063/1.1799251.

Jia, X., Walker, R.J., Kivelson, M.G., Khurana, K.K., Linker, J.A., 2008. Three-dimensional MHD simulations of Ganymede's magnetosphere. Journal of Geophysical Research (Space Physics) 113, A06212. doi:10.1029/2007JA012748.

Jia, X., Walker, R.J., Kivelson, M.G., Khurana, K.K., Linker, J.A., 2009. Properties of Ganymede's magnetosphere inferred from improved three-dimensional MHD simulations. Journal of Geophysical Research (Space Physics) 114, A09209. doi:10.1029/2009JA014375.

Joshipura, K.N., Vinodkumar, M., Patel, U.M., 2001. Electron impact total cross sections of CH_x, NH_x and OH radicals vis-à-vis their parent molecules. Journal of Physics B Atomic Molecular Physics 34, 509–519. doi:10.1088/0953-4075/34/4/301.

Kivelson, M.G., Bagenal, F., Kurth, W.S., Neubauer, F.M., Paranicas, C., Saur, J., 2004. Magnetospheric interactions with satellites. pp. 513–536.

Kivelson, M.G., Khurana, K.K., Coroniti, F.V., Joy, S., Russell, C.T., Walker, R.J., Warnecke, J., Bennett, L., Polanskey, C., 1997. Magnetic field and magnetosphere of Ganymede. Geophysical Research Letters 24, 2155. doi:10.1029/97GL02201.

Kivelson, M.G., Khurana, K.K., Russell, C.T., Walker, R.J., Warnecke, J., Coroniti, F.V., Polanskey, C., Southwood, D.J., Schubert, G., 1996. Discovery of Ganymede's magnetic field by the Galileo spacecraft. Nature 384, 537–541. doi:10.1038/384537a0.

Kliore, A.J., 1998. Satellite Atmospheres and Magnetospheres. Highlights of Astronomy 11, 1065.

Laher, R.R., Gilmore, F.R., 1990. Updated Excitation and Ionization Cross Sections for Electron Impact on Atomic Oxygen. Journal of Physical and Chemical Reference Data 19, 277–305. doi:10.1063/1.555872.

Leblanc, F., Oza, A.V., Leclercq, L., Schmidt, C., Cassidy, T., Modolo, R., Chaufray, J.Y., Johnson, R.E., 2017. On the orbital variability of Ganymede's atmosphere. Icarus 293, 185–198. doi:10.1016/j.icarus.2017.04.025.

Leclercq, L., Modolo, R., Leblanc, F., Hess, S., Mancini, M., 2016. 3D magnetospheric parallel hybrid multi-grid method applied to planet-plasma interactions. Journal of Computational Physics 309, 295–313. doi:10.1016/j.jcp.2016.01.005.

Marconi, M.L., 2007. A kinetic model of Ganymede's atmosphere. Icarus 190, 155–174. doi:10.1016/j.icarus.2007.02.016.

McGrath, M.A., Jia, X., Retherford, K., Feldman, P.D., Strobel, D.F., Saur, J., 2013. Aurora on Ganymede. Journal of Geophysical Research (Space Physics) 118, 2043–2054. doi:10.1002/jgra.50122.

Molyneux, P.M., Nichols, J.D., Bannister, N.P., Bunce, E.J., Clarke, J.T., Cowley, S.W.H., Gérard, J.C., Grodent, D., Milan, S.E., Paty, C., 2018. Hubble Space Telescope Observations of Variations in Ganymede's Oxygen Atmosphere and Aurora. Journal of Geophysical Research (Space Physics) 123, 3777–3793. doi:10.1029/2018JA025243.

Neubauer, F.M., 1998. The sub-Alfvénic interaction of the Galilean satellites with the Jovian magnetosphere. Journal of Geophysical Research 103, 19843–19866. doi:10.1029/97JE03370.

Opal, C.B., Peterson, W.K., Beaty, E.C., 1971. Measurements of Secondary-Electron Spectra Produced by Electron Impact Ionization of a Num-

ber of Simple Gases. The Journal of Chemical Physics 55, 4100–4106. doi:10.1063/1.1676707.

Paranicas, C., Paterson, W.R., Cheng, A.F., Mauk, B.H., McEntire, R.W., Frank, L.A., Williams, D.J., 1999. Energetic particle observations near Ganymede. Journal of Geophysical Research 104, 17459–17470. doi:10.1029/1999JA900199.

Paterson, W.R., Frank, L.A., Ackerson, K.L., 1999. Galileo plasma observations at Europa: Ion energy spectra and moments. Journal of Geophysical Research 104, 22779–22792. doi:10.1029/1999JA900191.

Paty, C., Paterson, W., Winglee, R., 2008. Ion energization in Ganymede's magnetosphere: Using multifluid simulations to interpret ion energy spectrograms. Journal of Geophysical Research (Space Physics) 113, A06211. doi:10.1029/2007JA012848.

Paty, C., Winglee, R., 2006. The role of ion cyclotron motion at Ganymede: Magnetic field morphology and magnetospheric dynamics. Geophysical Research Letters 33, L10106. doi:10.1029/2005GL025273.

Plainaki, C., Milillo, A., Massetti, S., Mura, A., Jia, X., Orsini, S., Mangano, V., De Angelis, E., Rispoli, R., 2015. The H_2O and O_2 exospheres of Ganymede: The result of a complex interaction between the jovian magnetospheric ions and the icy moon. Icarus 245, 306–319. doi:10.1016/j.icarus.2014.09.018.

Schreier, R., Eviatar, A., Vasyliunas, V.M., Richardson, J.D., 1993. Modeling the Europa plasma torus. Journal of Geophysical Research 98, 21. doi:10.1029/93JA02585.

Schunk, R., Nagy, A., 2004. Ionospheres: Physics, Plasma Physics, and Chemistry. Cambridge Atmospheric and Space Science Series, Cambridge University Press.

Scudder, J.D., Sittler, E.C., Bridge, H.S., 1981. A survey of the plasma electron environment of Jupiter - A view from Voyager. Journal of Geophysical Research 86, 8157–8179. doi:10.1029/JA086iA10p08157.

Shematovich, V.I., 2016. Neutral atmosphere near the icy surface of Jupiter's moon Ganymede. Solar System Research 50, 262–280. doi:10.1134/S0038094616040067.

Skeel, R.D., Gear, C.W., 1992. Does variable step size ruin a symplectic integrator? Physica D Nonlinear Phenomena 60, 311–313. doi:10.1016/0167-2789(92)90247-K.

Stolte, W.C., He, Z.X., Cutler, J.N., Lu, Y., Samson, J.A.R., 1998. Dissociative Photoionization Cross Sections of N_2 and O_2 from 100 to 800 eV. Atomic Data and Nuclear Data Tables 69, 171. doi:10.1006/adnd.1998.0775.

Straub, H.C., Renault, P., Lindsay, B.G., Smith, K.A., Stebbings, R.F., 1996. Absolute partial cross sections for electron-impact ionization of H_2, N_2, and O_2 from threshold to 1000 eV. Physical Review A 54, 2146–2153. doi:10.1103/PhysRevA.54.2146.

Turc, L., Leclercq, L., Leblanc, F., Modolo, R., Chaufray, J.Y., 2014. Modelling Ganymede's neutral environment: A 3D test-particle simulation. Icarus 229, 157–169. doi:10.1016/j.icarus.2013.11.005.

Vasyliūnas, V.M., Eviatar, A., 2000. Outflow of ions from Ganymede: A reinterpretation. Geophysical Research Letters 27, 1347–1349. doi:10.1029/2000GL003739.

Verner, D.A., Ferland, G.J., Korista, K.T., Yakovlev, D.G., 1996. Atomic Data for Astrophysics. II. New Analytic FITS for Photoionization Cross Sections of Atoms and Ions. The Astrophysical Journal 465, 487. doi:10.1086/177435.

Vigren, E., Galand, M., 2013. Predictions of Ion Production Rates and Ion Number Densities within the Diamagnetic Cavity of Comet 67P/Churyumov-Gerasimenko at Perihelion. The Astrophysical Journal 772, 33. doi:10.1088/0004-637X/772/1/33.

Wang, L., Germaschewski, K., Hakim, A., Dong, C., Raeder, J., Bhattacharjee, A., 2018. Electron Physics in 3-D Two-Fluid 10-Moment Modeling of Ganymede's Magnetosphere. Journal of Geophysical Research (Space Physics) 123, 2815–2830. doi:10.1002/2017JA024761.

Williams, D.J., Mauk, B., McEntire, R.W., 1998. Properties of Ganymede's magnetosphere as revealed by energetic particle observations. Geophysical Research Letters 103, 17523–17534. doi:10.1029/98JA01370.

Woods, T.N., Eparvier, F.G., Bailey, S.M., Chamberlin, P.C., Lean, J., Rottman, G.J., Solomon, S.C., Tobiska, W.K., Woodraska, D.L.,

2005. Solar EUV Experiment (SEE): Mission overview and first results. Journal of Geophysical Research (Space Physics) 110, A01312. doi:10.1029/2004JA010765.

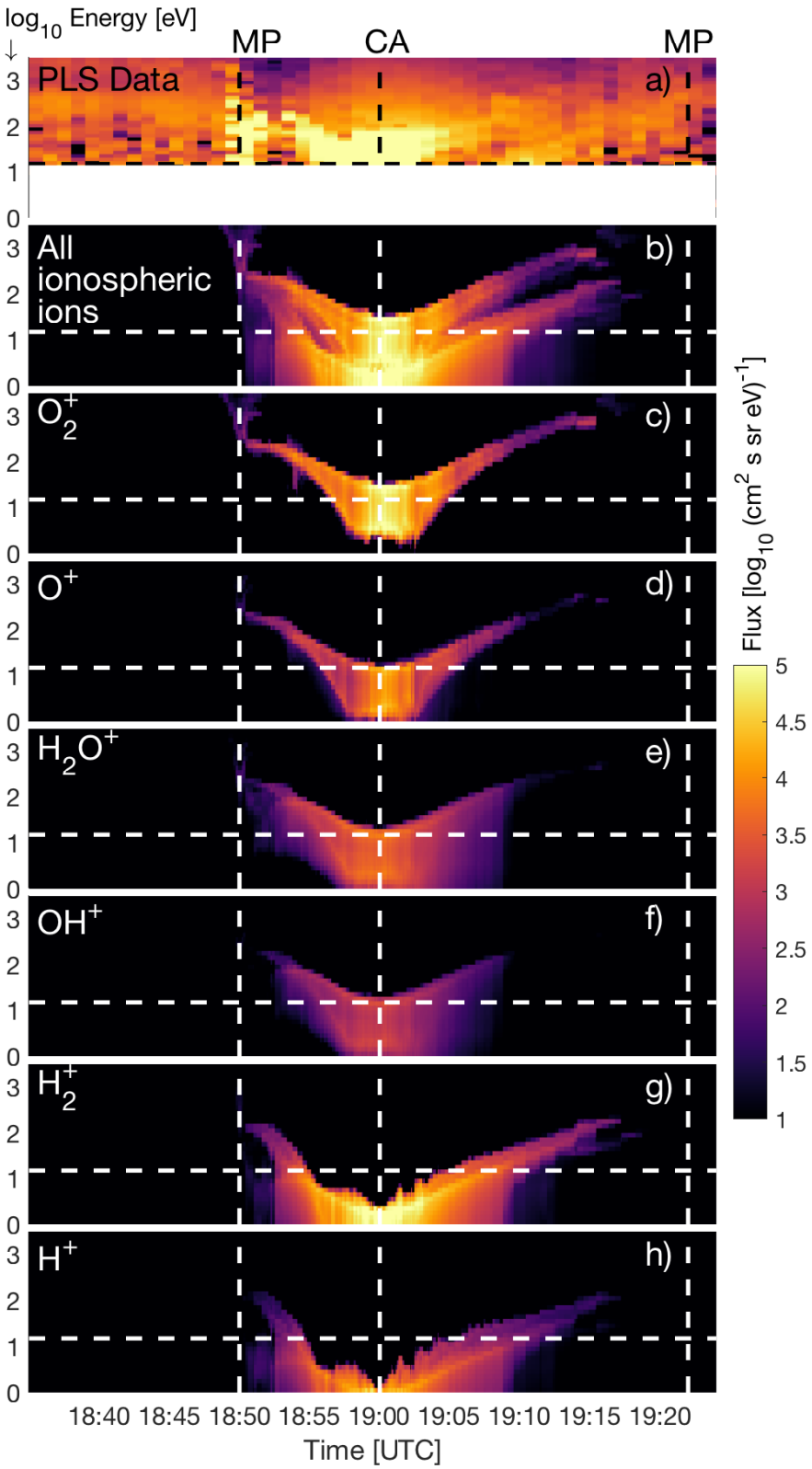

Figure D.14: Energy spectrum along the G2 flyby from: the PLS instrument (panel a), the ionospheric model considering all ionospheric species (panel b) and the ionospheric model separating the contribution from each different ionospheric species (panels c-h). The colour scale is logarithmic and equal for all panels. The white dashed horizontal lines indicate the energy below which the processing of the PLS dataset is considered unreliable. The white dashed vertical lines indicate the crossing times of the magnetopause (MP) and closest approach (CA).